On the spatial scale dependence of long-term persistence in global annual precipitation data and the Hurst Phenomenon

Enda O'Connell[1] , Greg O'Donnell[1], Demetris Koutsoyiannis[2]

[1] School of Engineering, Newcastle University, UK. [2] Department of Water Resources and Environmental Engineering, School of Civil Engineering, National Technical University of Athens.

Corresponding author: Enda O'Connell (enda.oconnell@ncl.ac.uk)

Key Points:

- For selected climatic regions, long-term persistence in gridded annual precipitation data increases with the spatial scale of averaging.
- Long-term persistence at the regional scale of averaging is linked to large scale modes of fluctuation in the climate system.
- Long-term persistence in basin average precipitation for the Blue Nile is shown to explain the Hurst Phenomenon for the Nile at Aswan.

Abstract

Precipitation deficits are the main physical drivers of droughts across the globe, and their level of persistence can be characterised by the Hurst coefficient H (0.5<H<1), with high H indicating strong long-term persistence (LTP). Previous analyses of point and gridded annual global precipitation datasets have concluded that LTP in precipitation is weak (H~0.6) which is inconsistent with higher values of H for large river basins e.g. the Nile. Based on an analysis of gridded annual precipitation data for eight selected regions distributed across the globe, an important new finding is that H increases with the spatial scale of averaging, with mean H values at the grid and regional scale of 0.66 and 0.83, respectively. The discovery of enhanced LTP at the regional scale of averaging of precipitation has important implications for characterising the severity of regional droughts, as well as LTP in the annual flows of large rivers and recharge to major aquifers. Teleconnections with known modes of low frequency variability in the global climate system are demonstrated using correlation analysis and stepwise regression. Despite having several constituent regions exhibiting LTP, the Northern Hemisphere surprisingly has no LTP; this is shown to result from different modes of low frequency climatic variability cancelling each other out. LTP for the Southern Hemisphere is moderate, and weak for Global average precipitation. LTP in Blue Nile basin scale precipitation is shown to explain the Hurst Phenomenon in naturalised annual flows for the River Nile, more than seventy years after its discovery by Hurst.

Plain Language Summary

In the 1950s, Harold Edwin Hurst, a British physicist and hydrologist, observed that the annual river Nile flows exhibited long-term persistence (LTP) where alternating periods of above and below average flows could be unusually long. He characterised LTP using a parameter H which increases from 0.5 (no LTP) up to a limit of 1, and found H of 0.90 for Nile flows. Analyses of long precipitation gauge records have typically given values of H in the range 0.55-0.60, leading some to conclude that precipitation could not account for the stronger LTP in the flows of the Nile and other large rivers. We analyse a long gridded global annual precipitation data set and find that, for eight selected regions, the average value of H increased from 0.66 at the grid scale to 0.83 at the regional scale of averaging. As flows in large rivers result from precipitation gathered over large upstream areas, this explains why the Nile exhibits LTP. Strong LTP at the regional scale is shown to be linked to known long-term fluctuations in the climate system. Our findings have important implications for characterising the risks of droughts which can extend over large areas.

1. Introduction

Long-term persistence (LTP) in geophysical time series, or the tendency of above or below average runs of years to be unusually long, was first quantified by Hurst (Hurst, 1951, 1956) using a coefficient H which characterizes LTP in the range 0.5<H<1, with H=0.5 corresponding to the independent (white noise) case i.e. no persistence. Hurst analysed a wide set of geophysical times series and found an average value of H=0.73, with a standard deviation of 0.09. In particular, he reported a value of H =0.9 for annual river Nile flows at Aswan, reflecting strong LTP. The disparity between these results, and the then current theory that predicted H=0.5 based on the increments of Brownian motion, has come to be known as the Hurst Phenomenon. Over the years, a number of stochastic approaches to modelling LTP have emerged (e.g., fractional Gaussian noise (Mandelbrot & Wallis, 1968, 1969), ARMA models (O'Connell,

1974a, 1974b), shifting mean models (Boes & Salas, 1978) and fractionally differenced models (Hosking, 1984)). Koutsoyiannis (2011a) has shown that those models exhibiting Hurst behaviour asymptotically can be encapsulated within a Hurst –Kolmogorov (HK) stochastic dynamics framework characterised by a simple scaling law, acknowledging the contribution of Kolmogorov who, unknown to Hurst and others, had developed the necessary theoretical basis in the 1940s. LTP is synonymous with Hurst-Kolmogorov behaviour and can be shown to arise from a complex dynamical system representation of a simple climate model (Mesa et al., 2012) or from maximum entropy considerations (Koutsoyiannis, 2011b, 2017).

The work of Hurst has been used to characterize LTP across multiple disciplines, ranging from climate science to the analysis of internet traffic and the flow of blood in human arteries (O'Connell et al., 2016). Recent research on Hurst behaviour in the climate and hydrology fields is reported by Adarsh et al. (2020); Adarsh and Priya (2021); Benavides-Bravo et al. (2021); Dimitriadis, Iliopoulou, et al. (2021); Dimitriadis, Koutsoyiannis, et al. (2021); Legates and Outcalt (2022); Pal et al. (2020); Rahmani and Fattahi (2021, 2022a, 2022b, 2022c). The hypothesis of long-term persistence (LTP) in annual precipitation has been explored in a number of studies of point and grid scale data. An analysis of annual precipitation records distributed over Europe with length above 200 years, as well as Climatic Research Unit (CRU) gridded data, yielded a mean value for H close to 0.6, suggesting weak LTP (Markonis & Koutsoyiannis, 2016). An analysis of a global annual precipitation data set from 1265 stations in which H was estimated using the aggregated variance method gave a mean H of 0.59, again suggesting weak LTP (Iliopoulou et al., 2018). A further analysis of a data set of 1535 records located mainly in the US, Europe and Australia in which H was estimated by maximum likelihood resulted in a median value of 0.56 (Tyralis et al., 2018). Bunde et al (2013) questioned whether LTP/memory exists in precipitation. LTP in near-surface air temperature records and long-term climate model simulations has been attributed to the existence of long-term memory in the climate system associated with ocean dynamics and ocean-atmosphere interactions (Fraedrich & Blender, 2003; Fraedrich et al., 2009; O'Connell et al., 2016).

Previous global mapping of H based on gridded precipitation data has shown that clusters of similar H values exist, albeit still reflecting weak LTP but with some high H patches (Rocheta et al., 2014). These clusters, the modelling of which has recently been demonstrated by Dimitriadis, Iliopoulou, et al. (2021), most likely reflect the influence of different modes of variability in the climate system such as the North Atlantic Oscillation (NAO), the Atlantic Multidecadal Oscillation (AMO), the Pacific Decadal Oscillation (PDO) etc. For example, a relationship has been established between the long-term variability of Nile river flows and sea surface temperature in the southern Indian Ocean and the eastern Pacific (Siam & Eltahir, 2015).

While the temporal scale dependence of LTP in precipitation records has been investigated by Markonis and Koutsoyiannis (2016), no such investigation has been conducted of dependence on the spatial scale of averaging. We report new findings on spatial scale dependence here, and its importance is twofold; (i) the LTP in the annual flows of large rivers has heretofore been unexplained, and (ii) major precipitation deficits and droughts occur at regional scales, and must therefore be governed by the level of LTP in regional scale precipitation. We demonstrate that LTP increases with the spatial scale of averaging of gridded global precipitation data, which provides important new understanding of how LTP in precipitation emerges at regional scales and of links with large scale climate fluctuations. This leads to a long-awaited explanation for the Hurst Phenomenon in the annual flows of the river Nile, and also sheds light on how regional

scale LTP exerts a major control over the intensity of regional precipitation deficits and droughts. Moreover, recharge to major aquifers occurs over large areas, and is also therefore affected by regional scale LTP. Our results can also be used for diagnostic checking of precipitation deficits in GCM baseline simulations.

In section 2.1, the data sets and regions analysed are described. Section 2.2 introduces the data sets and sources for river Nile flows. Section 2.3 describes the estimation of the Hurst coefficient using the climacogram, or aggregated scale analysis of the variance of the block mean. The spatial scale analysis of LTP and H is described in section 2.4, which is supported by Cumulative Departure from the Mean (CDM) plots in section 2.5. The use of correlation and stepwise regression analysis to analyse teleconnections is summarised in section 2.6. The Results are presented in section 3, followed by a Discussion in section 4 and some Conclusions in section 5.

2. Materials and Methods

2.1 Global precipitation data set and regions analysed

Our starting point is the Global Precipitation Climatology Centre (GPCC) global precipitation gridded data set (0.5x0.5 degree over land surfaces excluding Antarctica: version 7) for the period 1901-2013 (Schneider et al., 2015). We explore the spatial scale dependence of the Hurst coefficient H for a set of climatic regions distributed across the globe (Figure 1; after Harris et al. (2014)). These regions were originally chosen by Giorgi and Francisco (2000), and have been used by the IPCC in AR3 and AR4. They cover all of the global land areas approximately with a manageable number of previously defined climatic regions of rectangular shape to facilitate spatial aggregation.

2.2 River Nile annual flow data

Naturalised annual flow data for the Blue Nile and the White Nile for the period 1905-1994 have been digitised from plots in Sutcliffe and Parks (1999), while naturalised annual flows for the main Nile at Aswan for the period 1901-2013 have been digitised from a plot presented in Wheeler et al. (2020).

Figure 1. Regional grid scale annual average precipitation (1901-2013) (precipitation data from Schneider et al. (2015); regions defined in Harris et al. (2014)) . (Abbreviations: N., North; S., South; SE, Southeast, AM, America; AUS, Australia; EUR, Europe.)

2.3 Estimation of the Hurst coefficient

The Hurst coefficient H is widely accepted across multiple disciplines as the de facto parsimonious measure of LTP in time series. Here, H has been estimated using aggregated variance plot analysis (Beran, 1994) which is based on a property of the sample mean of a Hurst-Kolmogorov (HK) process (Koutsoyiannis, 2011a). For a HK time series split into nonoverlapping blocks of size *n*, the relationship between block size n and the variance of the block sample mean is given in equation (1) as:

$$\mathrm{var}(\bar{X}_n) = cn^{2H-2} \quad (1)$$

where $\bar{X}_n$ is the block sample mean, H is the Hurst coefficient, and c is a constant. Using a range of block sizes, a double log plot of the variance of the block sample mean against the block size is constructed, with the data points expected to fall along a line with negative slope 2H – 2 (e.g. see Figure S1). A slope of -1 indicates independence (white noise), with a long-range dependent HK process with H>0.5 having shallower slopes.

It should be noted that the term 'aggregated variance' is a misnomer as it is not the variance that is aggregated but the time scale; for this reason the term 'climacogram' has been coined to describe the double log plot (Koutsoyiannis, 2010).

The H values were calculated using the aggvarFit function in the R package fArma (Wuertz et al., 2017). The block sizes (denoted as m in fARMA) used in the calculation of the slope were the set of integer values in the range $4 \leq m \leq 14$. For the GPCC dataset, the maximum value of 14 provides eight values for calculation of the variance at the largest block size. The slope was obtained from the least square fit of the logarithm of the block sample mean variances versus the logarithm of the block sizes.

The standard variance estimator used in the R package fARMA has been shown to be biased (Tyralis & Koutsoyiannis, 2011), with the bias being a function of H. For H<0.7, the downward bias is negligible, but it becomes more noticeable above H=0.8. A comparison of results from the two estimators is presented in section 3.1.

2.4 Spatial scale analysis of LTP

We demonstrate the spatial scale analysis of LTP here for a region of the Sahel (Figure 2a) which is known for low frequency precipitation variability in the 20th century driven mainly by multi-decadal fluctuations in sea surface temperatures (SSTs) (Mohino et al., 2011). Figure 2 shows (a) a gridded (0.5x0.5degree) annual average precipitation map for a selected western region of the Sahel (area 3.19 km^{2}x10^6), and (b) corresponding gridded Hurst coefficients H. The grid average value of H is 0.73, reflecting moderate low frequency variability/long- term persistence at the grid scale. The gridded precipitation is then averaged across the region, and the resulting H value is found to be 0.9 (see Supplementary Fig. S1), indicating much stronger long-term persistence at the regional scale of averaging. The increase in H with spatial scale is shown in Figure 2c. Analyses for further selected regions in Figure 1 are presented in section 3.

Figure 2. (a) Gridded 0.5^o annual average precipitation (Schneider et al., 2015) for selected western region of the Sahel; (b) gridded H values for the same region; (c) spatial scale dependence of H; axis is in degrees.

2.5 Analysis of CDM plots

Cumulative Departure from the Mean (CDM) plots have been used to analyse different temporal patterns in LTP at the regional scale and to understand how regions combine to determine LTP at hemispheric and global scales of averaging. The CDM is defined in equation (2) as:

$$CDM_k = \sum_1^k X_t - k\bar{X} \quad (2)$$

where CDM_k is the CDM at time point k, $1 \leq k \leq n$ where n is the length of the time series, and $\bar{X}$ is the mean.

2.6 Correlation and regression analysis of teleconnections

A Pearson correlation matrix has been prepared showing linear dependencies between regional, hemispheric and global annual average precipitation. Stepwise linear regression has then been used to explore how much of the variance in global annual average precipitation can be explained by those regions exhibiting strong LTP at the regional scale of averaging, and their order according to significance. The stepwise linear regression was carried out using the R package Leaps (Lumley, 2017).

Pearson correlation analysis has also been used to explore linear dependencies between average annual regional precipitation and known large scale modes of variability in the global climate system (teleconnections: Chase et al. (2005)). Five indices of these modes of variability have been used as follows. In each case, an annual time series has been derived from the available monthly index data for the period 1901-2013.

The **North Atlantic Oscillation (NAO)** is one of the major modes of variability of the Northern Hemisphere atmosphere (Hurrell, 1995). It is particularly important in winter, when it exerts a strong control on the climate of the Northern Hemisphere (Osborn, 2011). This is also the season that exhibits strong interdecadal variability (Osborn, 2004). For winter, the difference between the normalised sea level pressure over Gibraltar and the normalised sea level pressure over Southwest Iceland is a useful index of the strength of the NAO. Jones et al. (1997) have used early instrumental data to extend this index back to 1823. The NAO data were obtained from the UK Climatic Research Unit (CRU).

The **Atlantic Multidecadal Oscillation (AMO)** reflects irregular multidecadal fluctuations in North Atlantic sea surface temperatures (SSTs), with alternating warm and cool periods. An irregular cycle has been identified for the AMO, with a period in the range 65-80 years (Kerr, 2000), but there is substantial residual variability. During AMO warmings, most of the United States sees less than normal precipitation, including Midwest droughts in the 1930s and 1950s (Enfield et al., 2001). An annual time series was derived from the monthly time series compiled by the National Oceanic and Atmospheric Administration (NOAA) which is based on North Atlantic SST averages, unsmoothed and not detrended (1856 to present, 1901-2013 analysed) and the climatology used (from the NOAA ERSST V2 SST, interpolated to a 5x5 grid)(Huang et al., 2017).

The **Southern Oscillation Index (SOI)** is a time series used to characterize the large scale sea level pressure (SLP) patterns in the tropical Pacific. Monthly mean SLP data at Tahiti [T] and Darwin [D] are used (Trenberth & NCAR Staff, 2022). The SOI is linked to large scale tropical SST variability and as such is a measure of the "SO" part of the El Niño–Southern Oscillation (ENSO) phenomenon. Extended periods of negative SOI correspond with El Nino events, characterized by warm SSTs in the eastern and central tropical Pacific. It has an irregular period of 2-8 years (Trenberth & NCAR Staff, 2022).

Monthly Darwin SLP data compiled by NOAA have been used to derive an annual time series for the period 1901-2013.

The **Pacific Decadal Oscillation (PDO)** is often described as a long-lived El Niño-like pattern of Pacific climate variability (Mantua & Hare, 2002; Zhang et al., 1997). As seen with the better-known El Niño/Southern Oscillation (ENSO), extremes in the PDO pattern are marked by widespread variations in the Pacific Basin and the North American climate. In parallel with the

ENSO phenomenon, the extreme phases of the PDO have been classified as being either warm or cool, as defined by ocean temperature anomalies in the northeast and tropical Pacific Ocean (Mantua & Hare, 2002). The NCEI PDO index is based on NOAA's extended reconstruction of SSTs (ERSST Version 5). An annual time series has been derived from the monthly ERSST PDO index.

The **Interdacadal Pacific Oscillation (IPO)** is an interdecadal quasi-oscillation seen mostly in the Pacific basin, but its impacts on surface temperature and precipitation have been found over Australia, the Southwest US and other regions. The PDO and IPO essentially capture the same interdecadal variability, with the PDO traditionally defined within the North Pacific while the IPO covers the whole Pacific basin (Dong & Dai, 2015). IPO Tripole Index (TPI) unfiltered data created at NOAA/ESRL PSD were used (Henley et al., 2015).

3. Results

3.1 Spatial scale dependence of LTP in regional precipitation

Following the analysis demonstrated for a region of the Sahel in section 2.4 above, the spatial scale dependence of H for a set of regions in Figure 1 is analysed. Eight regions were selected from the overall set, with average H values of 0.6 or greater for grid scale (0.5x0.5degree) precipitation, and exhibiting an increase in H with the scale of averaging; these regions are in general agreement with the clusters of higher grid scale H values observed by Rocheta et al. (2014) (a Global map of H is provided in Figure S2). The median area of these regions is 7.2 km^2x10^6. Five of the eight regions have weak LTP at the grid scale (H~0.6) (Table 1), while North Asia, Southern South America and Western Africa exhibit stronger grid scale LTP (H~0.70). In all cases, the H values for regional average precipitation are substantially higher than the medians of the grid scale values.

A comparison of the H estimates calculated using the aggvarFit function in fArma, and the unbiased estimator used by Tyralis and Koutsoyiannis (2011) yielded an average difference between the two sets of estimates of 0.02 which does not affect our main finding about the spatial scale dependence of H.

Table 1. (a) Median H values for regional grid scale precipitation and (b) average regional precipitation (Aggregated variance (climacogram; Koutsoyiannis, 2011a) plots are shown in Figure S3).

	Region	(a) Median H for grid scale precipitation	(b) H for average regional precipitation
1	Eastern North America	0.60	0.83
2	Amazon	0.63	0.72
3	Southern South America	0.69	0.78
4	Northern Europe	0.64	0.81
5	Western Africa	0.69	0.91
6	North Asia	0.78	0.99
7	Southern Asia	0.63	0.85
8	Southeast Asia	0.63	0.78
	Mean	**0.66**	**0.83**

Figure 3 presents box plots of the Hurst coefficient as a function of spatial scale for the regions listed in Table 1, starting at the (0.5x0.5 degree) grid scale. At each scale, the region was partitioned into non-overlapping tiles, with the Hurst coefficient estimated for the average precipitation for each tile (in calculating the regional average values, the grid scale values were weighted by their projected earth surface areas (Kelly & Šavrič, 2021)). That H increases with spatial scale is evident from all these plots, although in some cases, the increase with spatial scale only emerges when going from the 10x10 degree to the full regional scale. The results for North Asia are unusual in that they show relatively strong LTP at the grid scale (H = 0.78) and a H value close to 1 at the regional scale. This may be an artefact of the lower density of stations in this region used to derive the gridded precipitation values.

.

Figure 3. Box plots of H values for increasing scales of averaging of precipitation for the regions listed in Table 1 (The whiskers represent the 5^{th} and 95^{th} percentiles). Only tiles with more than 50% land were included .The x-axis is in degrees.

Some of the box plots suggest frequency distributions with negative skewnesses and a left tail of H values less than 0.5; however, they are small in number, and do not affect the overall averages significantly. They may reflect areas where relatively few measurements were available to derive the grid square precipitations.

3.2 LTP patterns at regional scale

For the 19 regions shown in Figure 1, time series plots of average regional precipitation are presented in Figure 4, overlain with cumulative departure from the mean (CDM) plots, and with Hurst coefficients added in the plot titles. The CDM plot is a useful diagnostic tool for revealing underlying runs of above and below average precipitation, the strength of which is reflected in the Hurst coefficient values. Of the set of 8 cases listed in Table 1, 4 exhibit similar CDM behaviour (Eastern North America, Southern South America, Northern Europe, North Asia) reflecting below average followed by above average fluctuations in regional precipitation. Western Africa shows the opposite behaviour, while Southern Asia and, to a lesser extent, Southeast Asia show some similarity to this. Amazon is largely dissimilar to the other members of the set.

Figure 4. Average annual regional precipitation (black) and cumulative departures from the mean (CDM) (red) time series plots for the period 1901-2013. Hurst coefficients are shown in parentheses in the plot titles.

Also shown in Figure 4 are plots for Northern Hemisphere (NH) (H= 0.5), Southern Hemisphere (SH) (H=0.7) and Global average precipitation (H=0.61). It is interesting that, while some regions of the NH (Eastern North America, Northern Europe, North Asia) show strong LTP (H > 0.8), the average precipitation of the entire NH does not exhibit persistence. The SH average precipitation exhibits moderate LTP (H=0.7) and there is weak global LTP (H=0.61) which emerges from the different LTP patterns for the two hemispheres. These latter results, and the CDM plots and Hurst coefficients, reflect the complex interacting influences of the climates of their constituent regions. We now explain why NH average precipitation does not exhibit persistence

3.3 LTP at hemispheric and global scales

Given that high H values have been obtained for several of the NH regions, it is surprising that H is 0.5 for the Northern Hemisphere when taken as a whole (Figure 4 and Table 2(a)). To explore how this emerges, the average precipitations for the regions in the NH have been combined progressively using area weighting, and the resulting CDM plots analysed. The calculation of the projected surface area of each 0.5 degree grid box of the GPCC data set has been performed using equation 1 from Kelly and Šavrič (2021). While typically, the range of grid box areas is small within a region, the range across the NH is large – e.g. those in North Asia are approximately one quarter the size of those at the Equator. This influences LTP at NH scale.

An investigation of LTP at hemispheric and global scales is important for two reasons. Firstly, an understanding of how LTP behaves at these scales represents a contribution to the field of global hydrology. Secondly, GCMs are known to be deficient in reproducing LTP and drought characteristics (e.g. Moon et al, 2018) so these results should be used to check baseline simulations of historical climates, from local to global scales. This issue is discussed in section 4.

The 5 regions of North America (Figure 1) are combined first using area weighting (equation 3):

$$\overline{X_t} = \sum_1^n A_i \; X_t^i / \sum_1^n A_i \qquad (3)$$

where $\overline{X_t}$ is the combined regional average precipitation for the n regions (n=5 for North America) for year t, and A_i and X_t^i are the constituent regional land areas and averages for year t. In Table 2a, the areas of the regional boxes and the land areas within each region are provided, together with the regional H estimates. The North America regions account for ~17% of the land area in the Northern Hemisphere. The Hurst coefficient for the aggregated area is 0.79 with a range 0.63-0.83 for the constituent regions (Table 2). This is referred to as Case 1. Figure 5a shows the CDM plots for the 5 North America regions and their weighted average (black). It is noted that 3 regions have similar CDM plots (Central North America, Eastern North America and Western North America) which accounts for the high H value for the aggregated area.

Table 2. (a) Areas of regional boxes (10^6km^2), land area within each regional box, and regional H estimates (* boxes have been clipped at the Equator for this analysis); (b) H estimates for aggregated areas – Cases 1-5.

(a)

Regional box	S	N	W	E	Regional box area	Land area	Fraction land (-)	H
Alaska	60	72	-170	-103	4.0	3.5	0.87	0.66
Central North America	30	50	-103	-85	3.4	3.4	0.99	0.63
Eastern North America	25	50	-85	-50	8.5	2.9	0.34	0.83
Western North America	30	60	-135	-103	8.3	5.8	0.70	0.68
Central America	10	30	-116	-83	7.6	3.0	0.40	0.63
Northern Europe	48	75	-10	40	7.9	5.2	0.65	0.81
Western Africa*	0	22	-20	18	10.1	7.4	0.73	0.91
Mediterranean	30	48	-10	40	8.6	6.2	0.72	0.65
Eastern Africa*	0	18	22	52	6.6	5.7	0.87	0.61
North Asia	50	70	40	180	17.2	14.7	0.86	0.99
Central Asia	30	50	40	75	6.6	6.3	0.96	0.58
Southern Asia	5	50	64	100	17.3	12.3	0.71	0.85
East Asia	20	50	100	145	13.5	8.6	0.63	0.52
Southeast Asia*	0	20	95	115	4.8	2.4	0.49	0.78
N Hemisphere	0	90	-180	180	255.0	111.5	0.44	0.50

(b)

	Case 1	Case 2	Case 3	Case 4	Case 5
H	0.79	0.50	0.75	0.78	0.58

334

335 **Figure 5.** (a) Cumulative departures from the mean (CDM:mm) plots for the North America
336 regions and the average for the regions (black); (b) CDM plots for North America (Case 1) and
337 combinations with other NH regions (Cases 2-5).

338 The previous analysis is repeated, but with the Northern Europe and Western Africa regions
339 included (Case 2), and the estimated Hurst coefficient is 0.50 (the West Africa area lying in the
340 SH has been excluded). This surprising result can be explained by inspecting the CDM plots for
341 Western Africa and North Europe (Figure 4). The Western Africa CDM has an opposite
342 fluctuation to the North American and Europe CDMs, so although all have high H values (Table
343 2), Western Africa apparently cancels out the North America and Northern Europe opposite
344 fluctuations (Figure 5b).

345 To complete the analysis, CDM plots have been prepared and H values have been estimated for the
346 following three cases:

347 Case 3: Case 2 + Mediterranean/Eastern Africa

348 Case 4: Case 3 + North Asia/Central Asia

349 Case 5: Case 4 + Southern Asia + East Asia + Southeast Asia

350 The corresponding CDM plots for Cases 3-5 are shown in Figure 5b, and the estimated H values
351 are 0.75, 0.78 and 0.58 respectively (Table 2b). Here, it can be seen that the Mediterranean and
352 East Africa regions have similar CDM plots which reinforce each other and introduce LTP into
353 the North Amerrica/North Europe/West Africa time series (Case 2) to give a H value of 0.75 for
354 Case 3. This is slightly reinforced by North Asia/Central Asia (Case 4) to give H = 0.78, but the
355 addition of Southern Asia and Southeast Asia (Case 5) which have CDM plots showing opposite
356 fluctuations results in a final H value of 0.58. Some of the NH land area has been excluded in
357 combining these regions so this result is consistent with the NH value of 0.50 (Figure 4).

358 In essence, the northern and southern regions of the NH have opposite fluctuations which cancel
359 each other out, resulting in no LTP for the NH. Precipitatation cannot be expected to increase in
360 one major part of the NH without being balanced by a reduction in another part, if the NH
361 overall shows no persistence . Of course all the underlying fluctuations are a function of the
362 sampled epoch, and other epochs would yield very different results, so a reminder of the huge
363 sampling variability associated with LTP. Moreover, as the epoch length is extended, longer term
364 fluctutations will become evident, as revealed by paleo records, but which can still be modelled
365 by a stationary HK stochastic process (Markonis and Koutsoyiannis, 2013)

366 A similar analysis for the SH would be expected to show that the Amazon region (H=0.72)
367 dominates the SH (H=0.70) (compare their CDM plots in Figure 4), resulting in H=0.61 for the
368 globe when the NH and SH are combined. The NH and SH regions are of course interconnected
369 and there are teleconnections between both hemispheres that are reflected in their respective H
370 values and the global H value. We now explore the role of teleconnections with known large
371 scale modes of variability in the climate system in explaining regional LTP, and their influences
372 on average hemispheric and global annual precipitation.

373 3.4 Influence of teleconnections on regional and global LTP

374 From the analysis presented in section 3.3, it is evident that the LTP regimes of the constituent
375 regions of the NH interact in a complex way to determine LTP at the NH scale. Here, we explore
376 the relationships between time series of average regional, hemispheric and global precipitation
377 to gain insight into how they interact over time. A correlation matrix has been prepared which
378 reveals the following (see supplementary Figure S4 which is based on the 8 regions exhibiting
379 strong LTP (Table 1), NH, LH and Global). Average Global precipitation is more highly
380 correlated with average Southern Hemisphere (SH) (Pearson r=0.82) than Northern Hemisphere
381 (NH) precipitation (r =0.69). NH precipitation shows significant positive correlations with all
382 regions (apart from Southern South America which is negatively correlated (r=-0.36), with
383 Southeast Asia (r=0.52) and Southern Asia (0.42) having the highest correlations. Amazon (r=0.
384 74) and Southeast Asia (r=0.43) are the most highly correlated regional variables with SH
385 precipitation. SH has a higher correlation with Global (r=0.82) than NH (r=0. 69). These latter
386 correlations may partially reflect the respective roles of LTP in SH (0.70) and NH precipitation
387 (H=0.50) in determining LTP in Global precipitation (H=0.61). However, the interactions
388 demonstrated graphically for the NH through the CDM plots in Figure 5 are apparently too
389 complex to decipher using the correlation analysis performed here.

390 Stepwise multiple linear regressions of the average Global precipitation time series on the
391 average precipitation time series for the 8 regions have been performed in which the best
392 combinations of the explanatory variables have been progressively identified (Table 3a).
393 Amazon is the best single explanatory variable (adjusted R^2=0.39); then Southeast Asia enters
394 (R^2= 0.61), followed by North Asia, Southern Asia, Western Africa, Northern Europe, Eastern
395 North America and Southern South America, with a final adjusted R^2= 0.72. Thus, 72% of the
396 variance of Global precipitation over the period 1901-2013 is explained by the 8 LTP regions
397 which underlines their important role in determining the temporal evolution of Global
398 precipitation.
399

Table 3. (a) Stepwise linear regression of average annual Global precipitation on annual regional precipitation (X denotes entry of an explanatory variable); (b) significant correlations between annual average regional precipitation and annual climatic indices for the period 1901-2013.

(a)

Adj R^2	Eastern N. AM	Amazon	Southern S. AM	Northern EUR	Western Africa	North Asia	Southern Asia	Southeast Asia
0.39		X						
0.61		X						X
0.63		X				X		X
0.67		X				X	X	X
0.70		X			X	X	X	X
0.71		X		X	X	X	X	X
0.71	X	X		X	X	X	X	X
0.72	X	X	X	X	X	X	X	X

(b)

Index	Eastern N. AM	Amazon	Southern S. AM	Northern EUR	Western Africa	North Asia	Southern Asia	SE Asia	Global
AMO	-	-	-	0.19	-	0.24	-	0.26	0.23
NAO	-	-	-	-	-	-	-	-	-
PDO	-	-0.32	0.22	-	-0.21	-0.23	-	-0.21	-0.46
IPO	-	-0.57	0.52	-	-0.21	-	-0.24	-0.54	-
SOI	-	0.51	-0.51	-	0.27	-	0.25	0.52	0.72

Correlation analysis is now used to explore what links might exist between known modes of long-term variability in the climate system and average annual precipitation for the 8 LTP regions. It has been shown through long-term coupled atmosphere-ocean model simulations that long-term persistence in the climate system can be attributed to ocean dynamics which have memory (Fraedrich & Blender, 2003; Fraedrich et al., 2009; O'Connell et al., 2016), and which are reflected in quasi-periodic oscillations in SSTs; these in turn are linked to long-term fluctuations in temperature, precipitation and runoff records across the globe (teleconnections; Chase et al., 2005)). Here we explore the correlations between regional precipitation and five

indices of these modes of variability: the Atlantic Multidecadal Oscillation (AMO), the North Atlantic Oscillation (NAO), the Pacific Decadal Oscillation (PDO), the Interdecadal Pacific Oscillation (IPO) and the Southern Oscillation Index (SOI) (section 2.6). Table 3b and Figure S4 present significant correlations with regional precipitation; NAO shows no significant correlation (its influence is on seasonal and spatial distribution: Kyte et al, 2006), while the IPO and SOI are inversely correlated as expected (Chiew & Leahy, 2003; McNeil & Cox, 2007). The Hurst coefficient for the AMO is 0.92; for the PDO, 0.85 and the SOI, 0.57, so the AMO and the PDO are the main drivers of LTP in regional precipitation (Figure S5). Time series of annual AMO, PDO and SOI values are shown in Figure S6 for the period 1900-2013 with CDM plots of each superposed, and also of annual Global precipitation. The correlations of Global precipitation with AMO, PDO and SOI are 0.23, -0.46 and 0.72 respectively, which suggests that the SOI (H=0.57) has a strong influence on the weak level of LTP in Global precipitation (H=0.61) (Figure S7 shows correlations at the grid scale). Stepwise linear regression of annual Global precipitation on AMO, PDO and SOI yields an adjusted R^2= 0.56. Therefore, by comparison with the results in Table 3(a), the 8 regions explain another 16% of the variance, but with 8 significant independent variables. As a direct comparison, the best three regions explain 63% of the variance (Amazon 39%;+Southeast Asia, 61%;+North Asia,63%) compared with 56% for the AMO. PDO and SOI. However, this is not a like-for-like comparison, as the H values for the two sets of explanatory variables are different, suggesting that other unknown explanatory factors may be affecting regional precipitation.

3.5 The Hurst Phenomenon explained for the river Nile

While LTP and the Hurst Phenomenon can be modelled stochastically using a H-K scaling law, an explanation of how the Hurst Phenomenon arises has proved more elusive. Based on our findings, it is suggested that the reason for the discrepancy between the weak LTP in point/grid-scale precipitation, and the higher H values observed in the naturalised annual flows of large river basins like the Nile, is the scale dependence of LTP in precipitation which is integrated/averaged by the basin with increasing spatial scale. We now provide the evidence that this is the case for the Nile.

The Blue Nile accounts for some 60-70% of annual Nile flows at Aswan. Figure 6a shows a boundary box surrounding the upper Blue Nile catchment while Figure 6b shows that H increases with the scale of averaging from 0.58 at the grid scale to 0.73 at the boundary box scale; the size of the boundary box does not allow a greater number of points to be displayed. Naturalised flows at Aswan, which incorporate the White Nile flows, yield H=0.66. For comparison, the original estimate used by Hurst, defined as

$$\mathrm{K} = Log(\frac{R}{S})/Log(\frac{n}{2}) \quad (4)$$

where R is the range of cumulative departures, S is the standard deviation and n is the sample size, has been calculated for comparison (Table 4), with K=0.71. The value of K=0.90 reported by Hurst (1951,1956) was for the shorter period 1870-1949, and reflected a sharp decline in the flows around 1900 which can be attributed to a widespread failure in tropical Monsoon precipitation around that time (Kraus, 1956).The White Nile flows reflect a different precipitation and LTP regime to the Blue Nile, and are modulated by Great Lake storage and evaporation in the Sudd region. The flows downstream from the Sudd at Malakal (Figure 6a) are therefore heavily damped with low variance and exhibit strong LTP (H =0.74; K=0.84) (Figure S8), and they account for around 30% of Nile flows at Aswan as year-round baseflow. Due to

opposing modes of climatic fluctuation in White Nile and Blue Nile flows (Figure S8), the H and K values for Aswan flows are reduced relative to those for Blue Nile precipitation (Table 4). Therefore, the CDM plots in Figure 7 and the coherence of the H and K values for precipitation and flows provide compelling evidence that the source of LTP in the Nile flows at Aswan is the LTP in Blue Nile basin precipitation. This finding is reinforced by the work of Siam and Eltahir (2015) who found that 44% of the variability of main Nile flows in the period July-October (the period of the Nile flood coming from the Blue Nile) could be explained through teleconnections with SSTs in the Southern Indian Ocean (SIO) and Eastern Pacific (ENSO). Moreover, during those years with anomalous SST conditions in both oceans, SIO and ENSO SST indices could collectively explain up to 84% of the interannual variability in main Nile flows in the flood season. It can therefore be deduced that Southern Indian Ocean and Eastern Pacific SSTs are the source of some of the LTP in Blue Nile precipitation. Figure 7 also shows that the time series and CDM plots for Blue Nile precipitation are remarkably similar to those for West Africa (Figure 4), suggesting that the teleconnection with SSTs in the southern Indian Ocean and eastern Pacific extends to West Africa and the Sahel, which were affected by the 1970s/1980s drought.

As long-term records for sub-catchments of the Blue Nile are not available, it is not possible to see how the LTP signal emerges in the flows with increasing scale, but the role of Blue Nile precipitation in explaining the LTP observed in downstream Nile flows at Aswan is clear.

Figure 6. (a) Boundary box for the Blue Nile catchment (black). Red polygons and labels depict: K - Blue Nile catchment at Khartoum, M – White Nile at Malakal and A – Nile at Aswan and (b) the scale dependence of H for precipitation averaged at increasing spatial scales for the period 1901-2013.

Table 4. Estimates of Hurst coefficient for Blue Nile boundary box annual precipitation and naturalised annual flows at Aswan, 1901-2013.

1901-2013	**H**	**K**
Blue Nile Box Precipitation	0.73	0.76
Nile Flows at Aswan	0.66	0.71

Figure 7. Time series and CDM plots for (a) Blue Nile boundary box annual precipitation; (b) annual Nile flows at Aswan, 1901-2013.

4. Discussion

In discussing the above results, we first want to qualify our use of the term 'trend'. Unless clear causal mechanisms for monotonically increasing or decreasing trends in a period of record can be identified, it is likely that such trends will be seen as parts of irregular low frequency movements at multidecadal/centennial and longer time scales that are evident in paleo records, in which case they are pseudo trends that are a function of the instrumental record length, and which are likely to undergo reversal in the following epoch. That anthropogenic climate change may be reflected in some of these apparent trends in recent decades is certainly possible, but,

based on the available evidence, the IPCC has concluded that natural climatic variability is still the dominant mode of variability governing precipitation deficits and droughts, and, by implication, LTP (Seneviratne et al., 2021). It should be noted that such variability is perfectly consistent with stationary Hurst-Kolmogorov (HK) dynamics and characterization using the Hurst coefficient H; indeed, it has been shown that HK dynamics can be used to characterize long term variability over times scales spanning nine orders of magnitude (Markonis & Koutsoyiannis, 2013).

The Hurst coefficients for regionally averaged precipitation for the 19 regions analysed show wide variation across the globe, with 8 regions showing evidence of strong LTP at the regional scale of averaging (Table 1: we have used $H>0.7$ to delineate the latter), and the remainder showing weak LTP. Eastern North America, Amazon and Southern South America all exhibit LTP, demonstrating some regional N-S structure. Northern Europe and North Asia both exhibit LTP and have coherent CDM plots, reflecting below average followed by above average fluctuations, appearing to suggest an upward trend. Western Africa shows strong LTP, but with the CDM plot indicating an opposite sequence of fluctuations/trend.

Identification of the spatial-scale dependence of LTP represents an important discovery that enhances understanding of the structure of long-term variability in regional precipitation. This is particularly important when characterizing the risk of regional scale droughts e.g. for the Sahel. Up to now, LTP in annual precipitation has been deemed to be weak based on the analysis of global point and pixel scale data sets, but is shown here to be enhanced considerably at the regional scale of averaging (for the eight selected regions, the mean H values at the grid and regional scales are 0.66 and 0.83, respectively). We venture that the reason for this is that point/local scale records are dominated by local climatic variability/noise which is a function of location. This is borne out by the findings of (Tyralis et al., 2018) who related H values for 1535 records to location and Köppen-Geiger climate class descriptors using a random forests algorithm; location emerged as the only significant explanatory variable. However, as precipitation is averaged over increasing spatial scales, it appears that the local scale variability/noise is largely averaged out, and that the underlying signal associated with large-scale long-term modes of variability in the climate system emerges progressively. This is not inconsistent with the modelling of LTP by weighting and aggregating short-range dependence processes (Granger & Joyeux, 1980; Koutsoyiannis, 2002; Mandelbrot, 1971), but the (possibly causal) link between LTP in regional precipitation and long-term variations in SSTs should be further investigated.

Although the Northern Hemisphere has several regions exhibiting strong LTP, it was a surprise to find that it is absent at the NH scale. However, examination of the CDM plots has shown that the different modes of long-term climatic variation affecting different regions effectively cancel each other out at the NH and Global scales. In analysing the 8 regions exhibiting strong LTP, no turnover in H at the scale of these regions has been observed, so the spheres of influence of the underlying climatic modes of variability is larger than the scales of the regions analysed. In the case of the teleconnection affecting the Blue Nile catchment, the sphere of influence stretches across the width of Africa to the Sahel. Mapping these spheres of influence would provide further insight into the possible links with SSTs in different oceanic regions.

The regression of average global precipitation on the eight average regional precipitations exhibiting LTP has explained 72% of the variance of Global precipitation, with Amazon and SE

Asia being the two most significant explanatory variables. Amazon, Southern South America and Southeast Asia all have highly significant correlations ($|r|>0.5$) with both the IPO and the SOI (and SOI and IPO are inversely correlated), showing spatial and temporal coherence between these modes of climatic variability and regional precipitation. The NH regions have weaker but significant correlations with AMO. The LTP for the SH ($H=0.7$) is associated with the PDO and the SOI, but even though LTP is strong for AMO ($H=0.92$) the correlation with NH regional precipitation is weak and LTP is absent from NH precipitation as a whole, even though it is strong for large regions thereof. The weak LTP in Global precipitation ($H=0.61$) reflects both the latter, and the stronger LTP in SH precipitation, but also the influence of the SOI which has weak LTP or even anti-persistence.

LTP for some long-term annual river flow records, such as the Nile (whose catchment covers about 10% of Africa, thus reflecting the climate of a big region), tends to be stronger than point/gridded annual precipitation data would suggest. Mudelsee (2007) has shown for a set of six river basins, including the Nile, that H increases with scale through the basin network. He reproduced this effect using gridded monthly precipitation to simulate the aggregation of monthly runoff through the river basin network, and attributed the increase in H to the network aggregation process, refuting the statement by Potter (1979) that "if long-term persistence in streamflow series has a physical basis, it must lie in the precipitation process." In reviewing the possible explanatory mechanisms for the Hurst Phenomenon, O'Connell et al. (2016) suggested that extended droughts synonymous with LTP in river flows must have their physical origin in the precipitation process, even if the LTP signal at the point/grid scale is weak. Based on our findings, it is hypothesised that the increase in LTP through the river basin network emerges primarily from the spatial scale dependence of precipitation which is integrated/averaged by the basin with increasing spatial scale, and which would appear to be implicitly embedded in Mudelsee's modelling, but not recognised as the reason for the modelled increase in river flow LTP with basin scale. Strong evidence in support of this hypothesis has been presented here for the case of the river Nile, explaining the Hurst Phenomenon more than 70 years after Hurst first identified it.

As with any analyses of LTP in finite samples, estimates of the Hurst coefficient are subject to considerable sampling variability, as the information content of a time series decrease with increasing H, as exemplified by equation 1. Nonetheless, our main finding that H is enhanced substantially at the regional scale relative to the grid scale is supported by averaging across eight regions which reduces substantially the sampling variability. Moreover, we have shown that the enhancement is linked to known long term modes of fluctuation in the climate system which further reinforces our finding. The explanation of the Hurst Phenomenon is based on clear coherence between the long-term pattern of variability in Blue Nile catchment precipitation and the Nile flows at Aswan, the consistency of the H estimates, and the link with SSTs demonstrated by Siam and Eltahir (2015).

To summarise, the identification of the spatial-scale dependence of LTP represents an important finding that enhances understanding of the structure of long-term variability in regional precipitation while also providing a long-awaited explanation of the Hurst Phenomenon for the river Nile. This is particularly important when characterizing the risk of regional scale droughts in precipitation and runoff. In a follow up paper (O'Connell et al., 2022), we have extended our analysis to the remaining 11 regions with grid scale $H<0.6$, and found that, while H increases with the spatial scale of averaging for 5 of these regions, the remainder showed no increase or a

585 slight decrease. We have presented an important theoretical finding which shows that if several
586 HK stochastic processes with different H values are averaged, the averaged process will assume
587 the largest H value asymptotically. This is not the case for finite sample time series where
588 opposing modes of climatic fluctuation over the sample epoch can cancel each other out, as
589 evidenced by the analysis in section 3.3. Furthermore, we have analysed the statistics of
590 precipitation deficits as a function of LTP, and found H to be a good parsimonious descriptor of
591 their durations and volumes (O'Connell et al., 2022). An analysis of standardised durations and
592 volumes averaged across all 19 regions in Figure 1 for the period 1901-2020 did not show any
593 evidence of intensification in recent decades that might be attributed to anthropogenic climate
594 change (ACC). This means that the dominant threat of precipitation deficits and droughts
595 historically has been from LTP and not ACC, and adaptation planning for the coming decades
596 should recognise this and be based on the full envelope of uncertainty synonymous with LTP and
597 HK stochastic dynamics, and not rely exclusively on GCM projections for the following reasons.

598 The reproduction of natural LTP by GCMs has been identified as deficient (Anagnostopoulos et
599 al., 2010; Johnson et al., 2011; Koutsoyiannis et al., 2008; Moon et al., 2018; Rocheta et al.,
600 2014) which represents an area of concern in assessing the severity of droughts under a future
601 climate (Ault et al., 2014). Additionally, a recent comprehensive study of the global
602 hydrological cycle (Koutsoyiannis, 2020) has suggested the presence of fluctuations, rather than
603 trends, and refuted IPCC's claims about a systematic intensification of the hydrological cycle.
604 This is reinforced by the findings of O'Connell et al (2022) on the statistics of precipitation
605 deficits discussed above. However, the findings in this paper can support diagnostic analyses of
606 LTP and drought severity in GCM baseline simulations, potentially leading to improved
607 projections of drought severity under possible future climates. In particular, GCMs should be
608 able to reproduce the scale dependent behaviour of LTP from local to global scales in baseline
609 simulations of historical climates.

610 For future work, modelling the evolution of LTP in the flows of large rivers as a function of
611 scale dependent LTP in average basin precipitation would provide valuable insight into how
612 LTP-driven droughts evolve in these river basins, and would support attribution analyses where
613 the effects of LTP are separated clearly from those of ACC.

614 ## 5. Conclusions

615 The main conclusions which can be drawn from our findings are:

616 1. Gridded annual precipitation for nineteen rectangular regions distributed across the globe
617 (GPCC version 7: 1901-2013) have been analysed for long-term persistence (LTP) using
618 the Hurst coefficient, and eight regions have been shown to exhibit moderate LTP at the
619 (0.5x0.5 degree) grid scale, with a mean H of 0.66.
620 2. A major finding is that the Hurst coefficient increases progressively with the spatial scale
621 of averaging of annual precipitation, to reveal much stronger LTP at the regional scale,
622 with mean H found to be 0.83.
623 3. A second major finding is that the Hurst Phenomenon for the annual Nile flows at Aswan
624 can be explained by the enhanced LTP in average precipitation for the Blue Nile
625 catchment, and not network aggregation as has previously been asserted.
626 4. Teleconnections between annual precipitation in the eight regions and known large scale
627 modes of variability in the climate system are analysed, and significant correlations are

found with the AMO, the PDO, the IPO and the SOI (the latter two being inversely correlated), reflecting long-term fluctuations in sea surface temperatures (SSTs).

5. Stepwise linear regressions of average global precipitation on average precipitation for the eight regions yields an explained variance of 72%, demonstrating their significant influence on average global precipitation. Regressing global precipitation on the AMO, PDO and SOI explains 56% of the variance.
6. LTP in average annual Northern Hemisphere (NH) precipitation is missing (H=0.5), despite having a number of regions with strong LTP. LTP is stronger for the SH (0.70), and is weak at the Global scale (H=0.61).
7. By analysing cumulative departure from the mean (CDM) plots and combining NH regions using area weighting, it is shown the long-term fluctuations in northern and southern NH regional precipitations effectively cancel each other out, resulting in no LTP at the NH scale. Global LTP reflects the relative influences of SH and NH precipitation.
8. Several studies have shown that the reproduction of LTP by GCMs is deficient, and the results presented here could support diagnostic analyses of GCM simulations of regional historical precipitation, and therefore serve to improve predictions of drought severity in future climates.

Acknowledgements

Greg O'Donnell was supported by the Water Security and Sustainable Development Hub, funded by the UK Research and Innovation Global Challenges Research Fund (ES/S008179/1). Useful comments were provided by two anonymous referees.

Open Research

The GPCC global precipitation gridded data set (0.5x0.5 degree over land surfaces excluding Antarctica: version 7) was used in the creation of this manuscript (Schneider et al., 2015). The NAO data were obtained from the UK Climatic Research Unit (CRU, 2018), the AMO data from the Physical Sciences Laboratory (PSL, 2018), the SOI data from the National Center for Atmospheric Research (NCAR, 2018), the PDO data from the National Centers for Environmental Information (NCEI, 2018) and the IPO Tripole Index (TPI) unfiltered data from PSL (Henley et al., 2015).

Blue Nile annual flows at Khartoum and White Nile annual Flows at Malakal for the period 1905-1994 have been digitised from plots in Sutcliffe and Parks (1999; Figures 8.3 and 9.8), while naturalised annual flows for the main Nile at Aswan for the period 1901-2013 have been digitised from a plot presented in Wheeler et al. (2020; Figure 2).

Estimates of the Hurst coefficient H were made using the fARMA R package (Wuertz et al., 2017), available under the General Public License 2 (GPL-2). The stepwise linear regressions, Table 3, were carried out using the R package Leaps (Lumley, 2017), available under GPL-2. R version 3.5.1 (GPL-2) was used with fARMA and Leaps (R Core Team, 2021). Figures were made using Matplotlib (Hunter, 2007) with Python version 2.7 (Python Software Foundation, 2020), available under the Python Software Foundation License (PSFL), with the exception of Figures S1, S3 and S5 which were made in R using the fARMA package (Wuertz et al., 2017).

References

669 Adarsh, S., Nourani, V., Archana, D. S., & Dharan, D. S. (2020). Multifractal description of
670 daily rainfall fields over India. *Journal of Hydrology, 586*, 124913.
671 https://www.sciencedirect.com/science/article/pii/S0022169420303735

672 Adarsh, S., & Priya, K. L. (2021). Multifractal Description of Droughts in Western India Using
673 Detrended Fluctuation Analysis. In A. Pandey, S. K. Mishra, M. L. Kansal, R. D. Singh, & V. P.
674 Singh (Eds.), *Hydrological Extremes: River Hydraulics and Irrigation Water Management* (pp.
675 133-142). Cham: Springer International Publishing.

676 Anagnostopoulos, G. G., Koutsoyiannis, D., Christofides, A., Efstratiadis, A., & Mamassis, N.
677 (2010). A comparison of local and aggregated climate model outputs with observed data.
678 *Hydrological Sciences Journal, 55*(7), 1094-1110.
679 https://doi.org/10.1080/02626667.2010.513518

680 Ault, T. R., Cole, J. E., Overpeck, J. T., Pederson, G. T., & Meko, D. M. (2014). Assessing the
681 Risk of Persistent Drought Using Climate Model Simulations and Paleoclimate Data. *Journal of*
682 *Climate, 27*(20), 7529-7549. https://journals.ametsoc.org/view/journals/clim/27/20/jcli-d-12-
683 00282.1.xml

684 Benavides-Bravo, F. G., Martinez-Peon, D., Benavides-Ríos, Á. G., Walle-García, O., Soto-
685 Villalobos, R., & Aguirre-López, M. A. (2021). A Climate-Mathematical Clustering of Rainfall
686 Stations in the Río Bravo-San Juan Basin (Mexico) by Using the Higuchi Fractal Dimension and
687 the Hurst Exponent. *Mathematics, 9*(21). Retrieved from doi:10.3390/math9212656

688 Beran, J. (1994). *Statistics for Long-Memory Processes*: Routledge.

689 Boes, D. C., & Salas, J. D. (1978). Nonstationarity of the mean and the hurst Phenomenon.
690 *Water Resources Research, 14*(1), 135-143.
691 https://agupubs.onlinelibrary.wiley.com/doi/abs/10.1029/WR014i001p00135

692 Bunde, A., Büntgen, U., Ludescher, J., Luterbacher, J., & von Storch, H. (2013). Is there
693 memory in precipitation? *Nature Climate Change, 3*(3), 174-175.
694 https://doi.org/10.1038/nclimate1830

695 Chase, T. N., Pielke Sr, R. A., & Avissar, R. (2005). Teleconnections in the Earth System. In
696 *Encyclopedia of Hydrological Sciences*.

697 Chiew, F. H. S., & Leahy, M. J. (2003). *Inter-decadal Pacific oscillation modulation of the*
698 *impact of El Niño/Southern Oscillation on Australian rainfall and streamflow*. Paper presented at
699 the MODSIM 2003: International Congress on Modelling and Simulation, Townsville, Australia.

700 CRU. (2018). North Atlantic Oscillation (NAO). [Dataset]. Climatic Research Unit. Accessed
701 June, 2018. https://crudata.uea.ac.uk/cru/data/nao/nao.dat.

702 Dimitriadis, P., Iliopoulou, T., Sargentis, G.-F., & Koutsoyiannis, D. (2021). Spatial Hurst–
703 Kolmogorov Clustering. *Encyclopedia, 1*(4), 1010-1025. https://www.mdpi.com/2673-
704 8392/1/4/77

705 Dimitriadis, P., Koutsoyiannis, D., Iliopoulou, T., & Papanicolaou, P. (2021). A Global-Scale
706 Investigation of Stochastic Similarities in Marginal Distribution and Dependence Structure of
707 Key Hydrological-Cycle Processes. *Hydrology, 8*(2). Retrieved from
708 doi:10.3390/hydrology8020059

709 Dong, B., & Dai, A. (2015). The influence of the Interdecadal Pacific Oscillation on
710 Temperature and Precipitation over the Globe. *Climate Dynamics, 45*(9), 2667-2681.
711 https://doi.org/10.1007/s00382-015-2500-x

712 Enfield, D. B., Mestas-Nuñez, A. M., & Trimble, P. J. (2001). The Atlantic Multidecadal
713 Oscillation and its relation to rainfall and river flows in the continental U.S. *Geophysical*
714 *Research Letters, 28*(10), 2077-2080.
715 https://agupubs.onlinelibrary.wiley.com/doi/abs/10.1029/2000GL012745

716 Fraedrich, K., & Blender, R. (2003). Scaling of Atmosphere and Ocean Temperature
717 Correlations in Observations and Climate Models. *Physical Review Letters, 90*(10), 108501.
718 https://link.aps.org/doi/10.1103/PhysRevLett.90.108501

719 Fraedrich, K., Blender, R., & Zhu, X. (2009). Continuum climate variability: Long-term
720 memory, scaling, and 1/f-noise. *International Journal of Modern Physics B, 23*(28n29), 5403-
721 5416. https://doi.org/10.1142/S0217979209063729

722 Giorgi, F., & Francisco, R. (2000). Evaluating uncertainties in the prediction of regional climate
723 change. *Geophysical Research Letters, 27*(9), 1295-1298.
724 https://doi.org/10.1029/1999GL011016. https://doi.org/10.1029/1999GL011016

725 Granger, C. W. J., & Joyeux, R. (1980). An introduction to long-memory time series models and
726 fractional differencing. *Journal of Time Series Analysis, 1*(1), 15-29.
727 https://onlinelibrary.wiley.com/doi/abs/10.1111/j.1467-9892.1980.tb00297.x

728 Harris, I., Jones, P. D., Osborn, T. J., & Lister, D. H. (2014). Updated high-resolution grids of
729 monthly climatic observations – the CRU TS3.10. *International Journal of Climatology, 34*(3),
730 623-642. https://rmets.onlinelibrary.wiley.com/doi/abs/10.1002/joc.3711

731 Henley, B. J., Gergis, J., Karoly, D. J., Power, S., Kennedy, J., & Folland, C. K. (2015). A
732 Tripole Index for the Interdecadal Pacific Oscillation. Climate Dynamics, 45(11-12), 3077-3090.
733 http://dx.doi.org/10.1007/s00382-015-2525-1. [Dataset]. Accessed June 2018.
734 https://psl.noaa.gov/data/timeseries/IPOTPI/

735 Hosking, J. R. M. (1984). Modeling persistence in hydrological time series using fractional
736 differencing. *Water Resources Research, 20*(12), 1898-1908.
737 https://agupubs.onlinelibrary.wiley.com/doi/abs/10.1029/WR020i012p01898

738 Huang, B., Thorne, P. W., Banzon, V. F., Boyer, T., Chepurin, G., Lawrimore, J. H., et al.
739 (2017). *NOAA Extended Reconstructed Sea Surface Temperature (ERSST), Version 5.*

740 Hunter, J. D. (2007). Matplotlib: A 2D Graphics Environment. *Computing in Science &*
741 *Engineering, 9*(3), 90-95.

742 Hurrell, J. W. (1995). Decadal Trends in the North Atlantic Oscillation: Regional Temperatures
743 and Precipitation. *Science, 269*(5224), 676-679.
744 https://www.science.org/doi/abs/10.1126/science.269.5224.676

745 Hurst, H. E. (1951). Long-Term Storage Capacity of Reservoirs. *Transactions of the American*
746 *Society of Civil Engineers, 116*(1), 770-799.
747 https://ascelibrary.org/doi/abs/10.1061/TACEAT.0006518

748 Hurst, H. E. (1956). Methods of using long-term storage in reservoirs. *Proceedings of the*
749 *Institution of Civil Engineers, 5*(5), 519-543.
750 https://www.icevirtuallibrary.com/doi/abs/10.1680/iicep.1956.11503

751 Iliopoulou, T., Papalexiou, S. M., Markonis, Y., & Koutsoyiannis, D. (2018). Revisiting long-
752 range dependence in annual precipitation. *Journal of Hydrology, 556*, 891-900.
753 https://www.sciencedirect.com/science/article/pii/S0022169416301962

754 Johnson, F., Westra, S., Sharma, A., & Pitman, A. J. (2011). An Assessment of GCM Skill in
755 Simulating Persistence across Multiple Time Scales. *Journal of Climate, 24*(14), 3609-3623.
756 https://journals.ametsoc.org/view/journals/clim/24/14/2011jcli3732.1.xml

757 Jones, P. D., Jonsson, T., & Wheeler, D. (1997). Extension to the North Atlantic oscillation using
758 early instrumental pressure observations from Gibraltar and south-west Iceland. *International*
759 *Journal of Climatology, 17*(13), 1433-1450.
760 https://rmets.onlinelibrary.wiley.com/doi/abs/10.1002/%28SICI%291097-
761 0088%2819971115%2917%3A13%3C1433%3A%3AAID-JOC203%3E3.0.CO%3B2-P

762 Kelly, K., & Šavrič, B. (2021). Area and volume computation of longitude–latitude grids and
763 three-dimensional meshes. *Transactions in GIS, 25*(1), 6-24.
764 https://onlinelibrary.wiley.com/doi/abs/10.1111/tgis.12636

765 Kerr, R. A. (2000). A North Atlantic Climate Pacemaker for the Centuries. *Science, 288*(5473),
766 1984-1985. https://www.science.org/doi/abs/10.1126/science.288.5473.1984

767 Koutsoyiannis, D. (2002). The Hurst phenomenon and fractional Gaussian noise made easy.
768 *Hydrological Sciences Journal, 47*(4), 573-595. https://doi.org/10.1080/02626660209492961

769 Koutsoyiannis, D. (2010). HESS Opinions "A random walk on water". *Hydrol. Earth Syst. Sci.,*
770 *14*(3), 585-601. https://hess.copernicus.org/articles/14/585/2010/

771 Koutsoyiannis, D. (2011a). Hurst-Kolmogorov Dynamics and Uncertainty. *JAWRA Journal of*
772 *the American Water Resources Association, 47*(3), 481-495.
773 https://onlinelibrary.wiley.com/doi/abs/10.1111/j.1752-1688.2011.00543.x

774 Koutsoyiannis, D. (2011b). Hurst–Kolmogorov dynamics as a result of extremal entropy
775 production. *Physica A: Statistical Mechanics and its Applications, 390*(8), 1424-1432.
776 https://EconPapers.repec.org/RePEc:eee:phsmap:v:390:y:2011:i:8:p:1424-1432

777 Koutsoyiannis, D. (2017). Entropy Production in Stochastics. *Entropy, 19*(11), 581.
778 https://www.mdpi.com/1099-4300/19/11/581

779 Koutsoyiannis, D. (2020). Revisiting the global hydrological cycle: is it intensifying? *Hydrol.*
780 *Earth Syst. Sci., 24*(8), 3899-3932. https://hess.copernicus.org/articles/24/3899/2020/

781 Koutsoyiannis, D., Efstratiadis, A., Mamassis, N., & Christofides, A. (2008). On the credibility
782 of climate predictions. *Hydrological Sciences Journal, 53*(4), 671-684.
783 https://doi.org/10.1623/hysj.53.4.671

784 Legates, D. R., & Outcalt, S. I. (2022). Detection of climate transitions and discontinuities by
785 Hurst rescaling. *International Journal of Climatology, 42*(9), 4753-4772.
786 https://doi.org/10.1002/joc.7502. https://doi.org/10.1002/joc.7502

787 Lumley, T. (2017). leaps: Regression Subset Selection. R package version 3.0 (based on Fortran
788 code by Alan Miller). [Software]. *https://CRAN.R-project.org/package=leaps*.

789 Mandelbrot, B. B. (1971). A Fast Fractional Gaussian Noise Generator. *Water Resources*
790 *Research, 7*(3), 543-553.
791 https://agupubs.onlinelibrary.wiley.com/doi/abs/10.1029/WR007i003p00543

792 Mandelbrot, B. B., & Wallis, J. R. (1968). Noah, Joseph, and Operational Hydrology. *Water*
793 *Resources Research, 4*(5), 909-918.
794 https://agupubs.onlinelibrary.wiley.com/doi/abs/10.1029/WR004i005p00909

795 Mandelbrot, B. B., & Wallis, J. R. (1969). Computer Experiments With Fractional Gaussian
796 Noises: Part 1, Averages and Variances. *Water Resources Research, 5*(1), 228-241.
797 https://agupubs.onlinelibrary.wiley.com/doi/abs/10.1029/WR005i001p00228

798 Mantua, N. J., & Hare, S. R. (2002). The Pacific Decadal Oscillation. *Journal of Oceanography,*
799 *58*(1), 35-44. https://doi.org/10.1023/A:1015820616384

800 Markonis, Y., & Koutsoyiannis, D. (2013). Climatic Variability Over Time Scales Spanning
801 Nine Orders of Magnitude: Connecting Milankovitch Cycles with Hurst–Kolmogorov Dynamics.
802 *Surveys in Geophysics, 34*(2), 181-207. https://doi.org/10.1007/s10712-012-9208-9

803 Markonis, Y., & Koutsoyiannis, D. (2016). Scale-dependence of persistence in precipitation
804 records. *Nature Climate Change, 6*, 399-401. https://doi.org/10.1038/nclimate2894

805 McNeil, V. H., & Cox, M. E. (2007). Defining the climatic signal in stream salinity trends using
806 the Interdecadal Pacific Oscillation and its rate of change. *Hydrol. Earth Syst. Sci., 11*(4), 1295-
807 1307. https://hess.copernicus.org/articles/11/1295/2007/

808 Mesa, O. J., Gupta, V. K., & O'Connell, P. E. (2012). Dynamical System Exploration of the
809 Hurst Phenomenon in Simple Climate Models. In A. S. Sharma, A. Bunde, V. P. Dimri, & D. N.
810 Baker (Eds.), *Extreme Events and Natural Hazards: The Complexity Perspective* (pp. 209-230).
811 Washington DC: American Geophysical Union.

812 Mohino, E., Janicot, S., & Bader, J. (2011). Sahel rainfall and decadal to multi-decadal sea
813 surface temperature variability. *Climate Dynamics, 37*(3), 419-440.
814 https://doi.org/10.1007/s00382-010-0867-2

815 Moon, H., Gudmundsson, L., & Seneviratne, S. I. (2018). Drought Persistence Errors in Global
816 Climate Models. *Journal of Geophysical Research: Atmospheres, 123*(7), 3483-3496.
817 https://agupubs.onlinelibrary.wiley.com/doi/abs/10.1002/2017JD027577

818 Mudelsee, M. (2007). Long memory of rivers from spatial aggregation. *Water Resources*
819 *Research, 43*(1). https://agupubs.onlinelibrary.wiley.com/doi/abs/10.1029/2006WR005721

820 NCAR. (2018). Southern Oscillation Indices: Signal, Noise and Tahiti/Darwin SLP (SOI).
821 [Dataset]. National Center for Atmospheric Rersearch. Accessed June, 2018.
822 https://climatedataguide.ucar.edu/climate-data/southern-oscillation-indices-signal-noise-and-
823 tahitidarwin-slp-soi.

824 NCEI. (2018). Pacific Decadal Oscillation (PDO). [Dataset]. National Centers for Environmental
825 Information. Accessed June, 2018. https://www.ncei.noaa.gov/access/monitoring/pdo/.

O'Connell, P. E. (1974a). *A simple stochastic modelling of Hurst's law.* Paper presented at the Proceedings of International Symposium on Mathematical Models in Hydrology, Warsaw.

O'Connell, P. E. (1974b). *Stochastic modelling of long-term persistence in streamflow sequences.* Imperial College, London,

O'Connell, P. E., Koutsoyiannis, D., Lins, H. F., Markonis, Y., Montanari, A., & Cohn, T. (2016). The scientific legacy of Harold Edwin Hurst (1880–1978). *Hydrological Sciences Journal, 61*(9), 1571-1590. https://doi.org/10.1080/02626667.2015.1125998

O'Connell, E., O'Donnell, G., & Koutsoyiannis, D. (2022). The Spatial Scale Dependence of The Hurst Coefficient in Global Annual Precipitation Data, and Its Role in Characterising Regional Precipitation Deficits within a Naturally Changing Climate. *Hydrology, 9*(11). Retrieved from doi:10.3390/hydrology9110199

Osborn, T. J. (2004). Simulating the winter North Atlantic Oscillation: the roles of internal variability and greenhouse gas forcing. *Climate Dynamics, 22*(6), 605-623. https://doi.org/10.1007/s00382-004-0405-1

Osborn, T. J. (2011). Winter 2009/2010 temperatures and a record-breaking North Atlantic Oscillation index. *Weather, 66*(1), 19-21.

Pal, S., Dutta, S., Nasrin, T., & Chattopadhyay, S. (2020). Hurst exponent approach through rescaled range analysis to study the time series of summer monsoon rainfall over northeast India. *Theoretical and Applied Climatology, 142*(1), 581-587. https://doi.org/10.1007/s00704-020-03338-6

Potter, K. W. (1979). Annual precipitation in the northeast United States: Long memory, short memory, or no memory? *Water Resources Research, 15*(2), 340-346. https://agupubs.onlinelibrary.wiley.com/doi/abs/10.1029/WR015i002p00340

PSL. (2018). AMO (Atlantic Multidecadal Oscillation) Index. [Dataset]. Physical Sciences Laboratory. Accessed June, 2018. https://psl.noaa.gov/data/timeseries/AMO/.

Python Software Foundation. (2020). Python Language Reference, version 2.7. [Software]. https://www.python.org/downloads/.

R Core Team. (2021). R: A language and environment for statistical computing. R Foundation for Statistical Computing. Vienna, Austria. [Software]. https://cran.r-project.org.

Rahmani, F., & Fattahi, M. H. (2021). A multifractal cross-correlation investigation into sensitivity and dependence of meteorological and hydrological droughts on precipitation and temperature. *Natural Hazards, 109*(3), 2197-2219. https://doi.org/10.1007/s11069-021-04916-1

Rahmani, F., & Fattahi, M. H. (2022a). Association between forecasting models' precision and nonlinear patterns of daily river flow time series. *Modeling Earth Systems and Environment, 8*(3), 4267-4276. https://doi.org/10.1007/s40808-022-01351-4

Rahmani, F., & Fattahi, M. H. (2022b). Exploring the association between anomalies and multifractality variations in river flow time series. *Hydrological Sciences Journal, 67*(7), 1084-1095. https://doi.org/10.1080/02626667.2022.2069503

Rahmani, F., & Fattahi, M. H. (2022c). The influence of rainfall time series fractality on forecasting models' efficiency. *Acta Geophysica, 70*(3), 1349-1361. https://doi.org/10.1007/s11600-022-00776-w

Rocheta, E., Sugiyanto, M., Johnson, F., Evans, J., & Sharma, A. (2014). How well do general circulation models represent low-frequency rainfall variability? *Water Resources Research, 50*(3), 2108-2123. https://agupubs.onlinelibrary.wiley.com/doi/abs/10.1002/2012WR013085

Schneider, U., Becker, A., Finger, P., Meyer-Christoffer, A., Rudolf, B., & Ziese, M. (2015). GPCC Full Data Monthly Product Version 7.0 at 0.5°: Monthly Land-Surface Precipitation from Rain-Gauges built on GTS-based and Historic Data. [Dataset]. Open Data Server of the German Meteorological Service (DWD). https://10.5676/DWD_GPCC/FD_M_V7_050.

Seneviratne, S. I., X. Zhang, M. Adnan, W. Badi, C. Dereczynski, A. Di Luca, et al. (2021). *Weather and Climate Extreme Events in a Changing Climate. In Climate Change 2021: The Physical Science Basis. Contribution of Working Group I to the Sixth Assessment Report of the Intergovernmental Panel on Climate Change, Section 11.6.1.1*. Retrieved from https://10.1017/9781009157896.013

Siam, M. S., & Eltahir, E. A. B. (2015). Explaining and forecasting interannual variability in the flow of the Nile River. *Hydrol. Earth Syst. Sci., 19*(3), 1181-1192. https://hess.copernicus.org/articles/19/1181/2015/

Sutcliffe, J. V., & Parks, Y. P. (1999). *The hydrology of the Nile. IAHS Special Publication 5*. Retrieved from Wallingford, UK:

Trenberth, K., & NCAR Staff. (2022). The Climate Data Guide: Southern Oscillation Indices: Signal, Noise and Tahiti/Darwin SLP (SOI). https://climatedataguide.ucar.edu/climate-data/southern-oscillation-indices-signal-noise-and-tahitidarwin-slp-soi. Last modified 17 Apr 2022.

Tyralis, H., Dimitriadis, P., Koutsoyiannis, D., O'Connell, P. E., Tzouka, K., & Iliopoulou, T. (2018). On the long-range dependence properties of annual precipitation using a global network of instrumental measurements. *Advances in Water Resources, 111*, 301-318. https://www.sciencedirect.com/science/article/pii/S0309170817309181

Tyralis, H., & Koutsoyiannis, D. (2011). Simultaneous estimation of the parameters of the Hurst–Kolmogorov stochastic process. *Stochastic Environmental Research and Risk Assessment, 25*(1), 21-33. https://doi.org/10.1007/s00477-010-0408-x

Wheeler, K. G., Jeuland, M., Hall, J. W., Zagona, E., & Whittington, D. (2020). Understanding and managing new risks on the Nile with the Grand Ethiopian Renaissance Dam. *Nature Communications, 11*(1), 5222. https://doi.org/10.1038/s41467-020-19089-x

Wuertz, D., Setz, T., & Chalabi, Y. (2017). fArma: Rmetrics - Modelling ARMA Time Series Processes. R package version 3042.81. [Software]. https://github.com/cran/fArma.

Zhang, Y., Wallace, J. M., & Battisti, D. S. (1997). ENSO-like Interdecadal Variability: 1900–93. *Journal of Climate, 10*(5), 1004-1020. https://journals.ametsoc.org/view/journals/clim/10/5/1520-0442_1997_010_1004_eliv_2.0.co_2.xml

Figure 1.

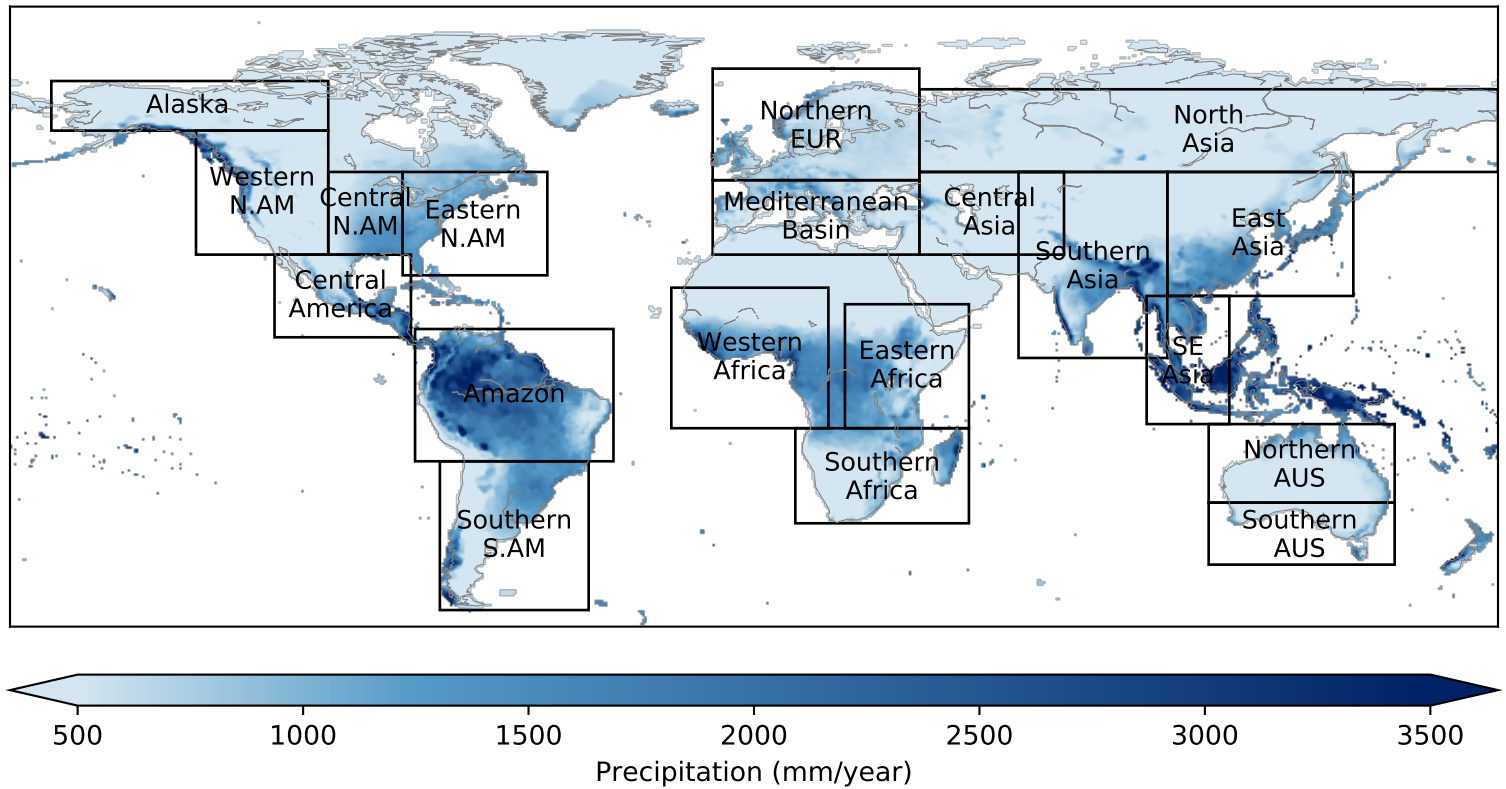
Alaska
Western N.AM
Central N.AM
Eastern N.AM
Central America
Amazon
Southern S.AM
Northern EUR
Mediterranean Basin
Western Africa
Eastern Africa
Southern Africa
Central Asia
North Asia
Southern Asia
East Asia
SE Asia
Northern AUS
Southern AUS
500
1000
1500
2000
2500
3000
3500
Precipitation (mm/year)

Figure 2.

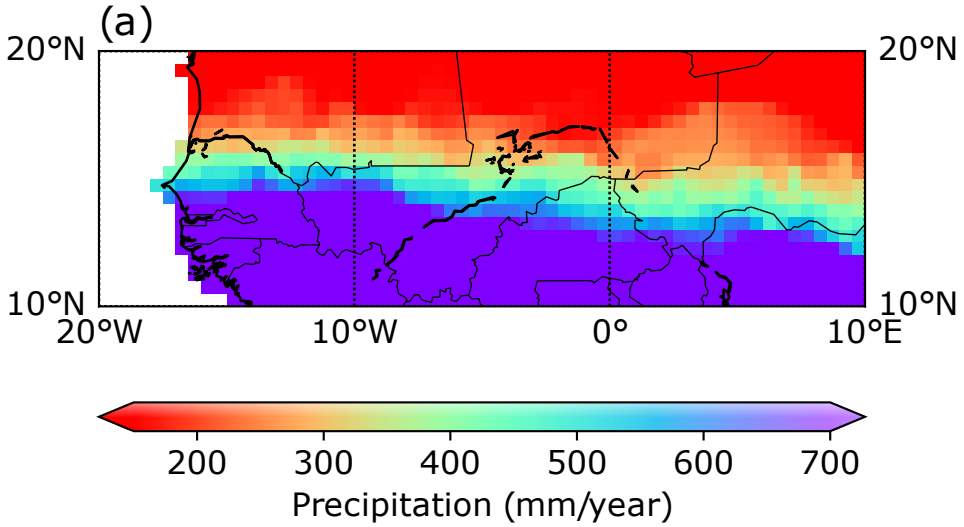
(a)
20°N
10°N
20°W
10°W
0°
10°E
200
300
400
500
600
700
Precipitation (mm/year)

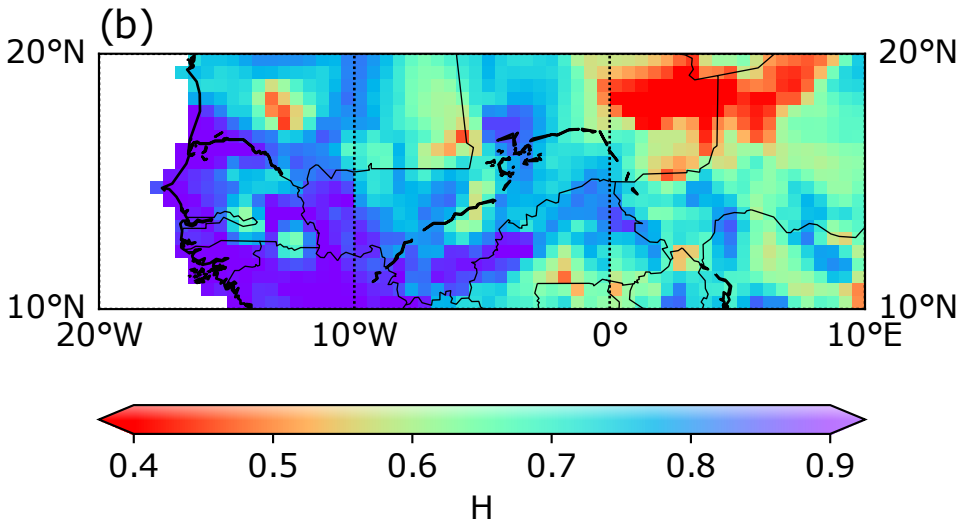
(b)
20°N
10°N
20°W
10°W
0°
10°E
0.4
0.5
0.6
0.7
0.8
0.9
H

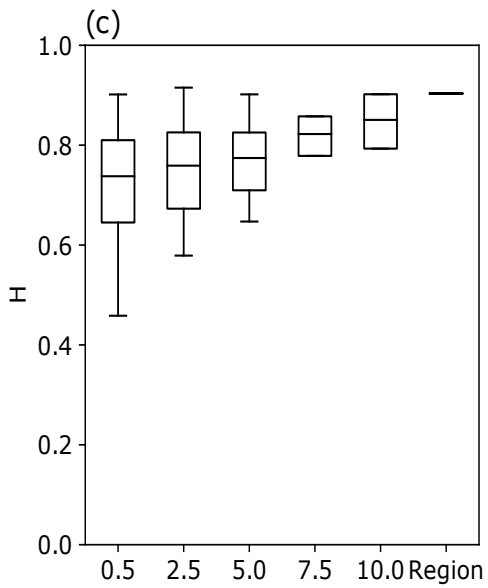
(c)
1.0
0.8
0.6
0.4
0.2
0.0
H
0.5
2.5
5.0
7.5
10.0
Region

Figure 3.

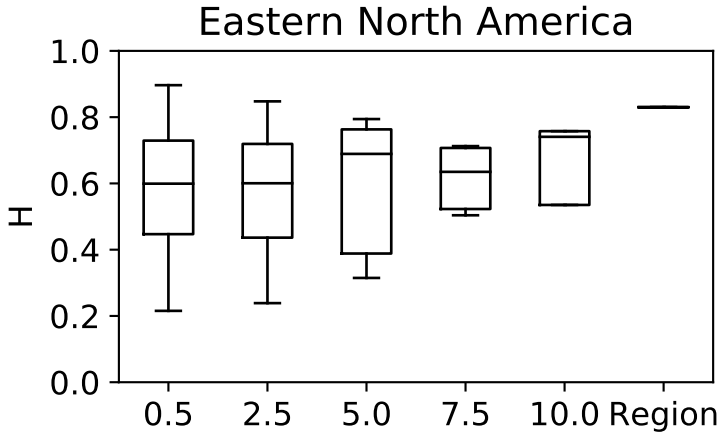
Eastern North America
H
1.0
0.8
0.6
0.4
0.2
0.0
0.5
2.5
5.0
7.5
10.0
Region

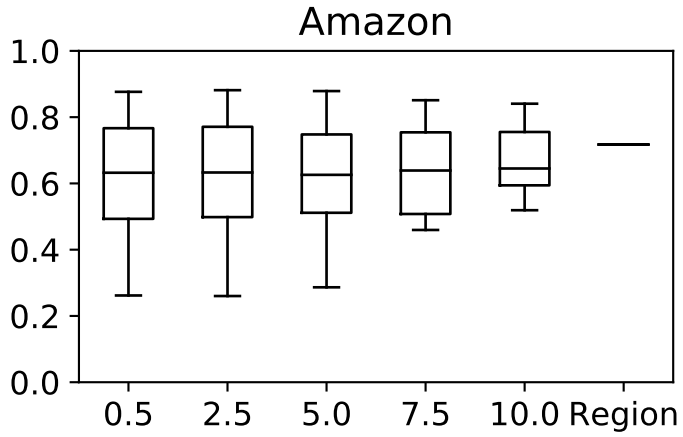
Amazon
1.0
0.8
0.6
0.4
0.2
0.0
0.5
2.5
5.0
7.5
10.0
Region

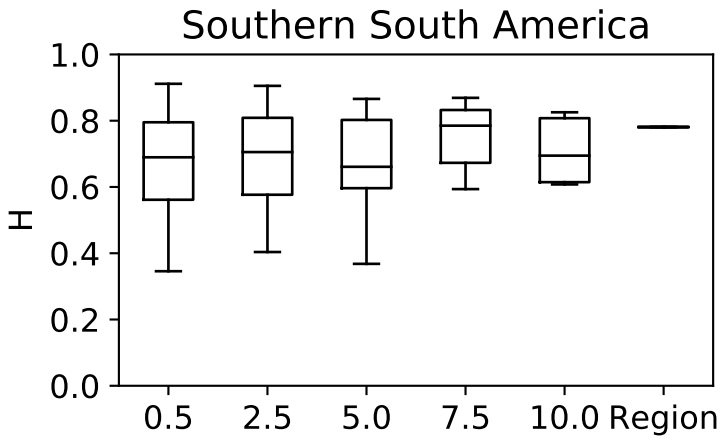
Southern South America
H
1.0
0.8
0.6
0.4
0.2
0.0
0.5
2.5
5.0
7.5
10.0
Region

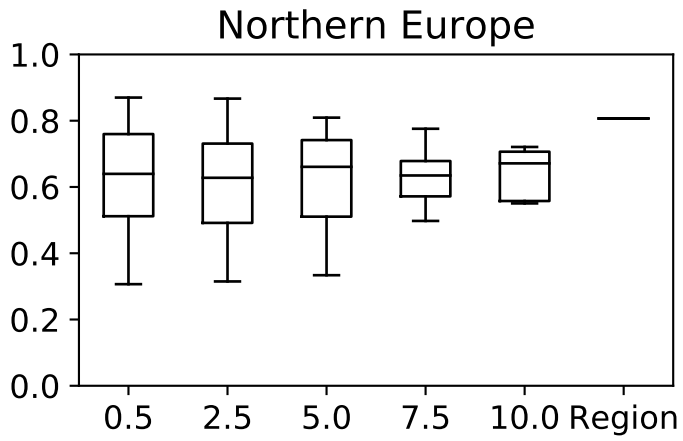
Northern Europe
1.0
0.8
0.6
0.4
0.2
0.0
0.5
2.5
5.0
7.5
10.0
Region

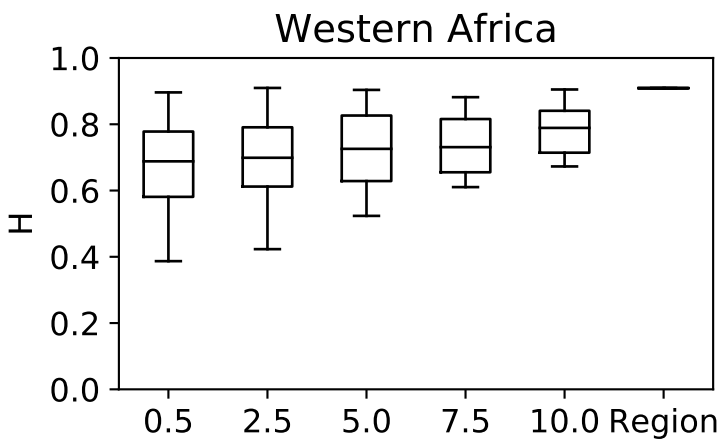
Western Africa
H
1.0
0.8
0.6
0.4
0.2
0.0
0.5
2.5
5.0
7.5
10.0
Region

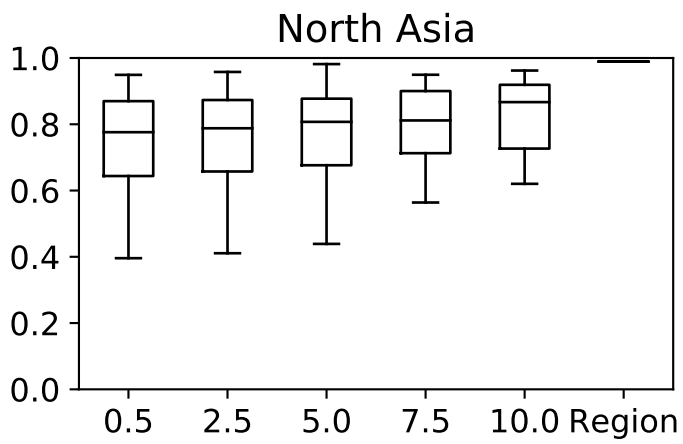
North Asia
1.0
0.8
0.6
0.4
0.2
0.0
0.5
2.5
5.0
7.5
10.0
Region

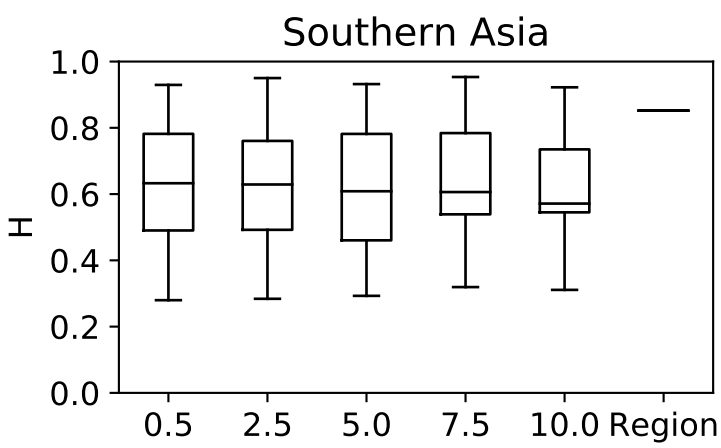
Southern Asia
H
1.0
0.8
0.6
0.4
0.2
0.0
0.5
2.5
5.0
7.5
10.0
Region

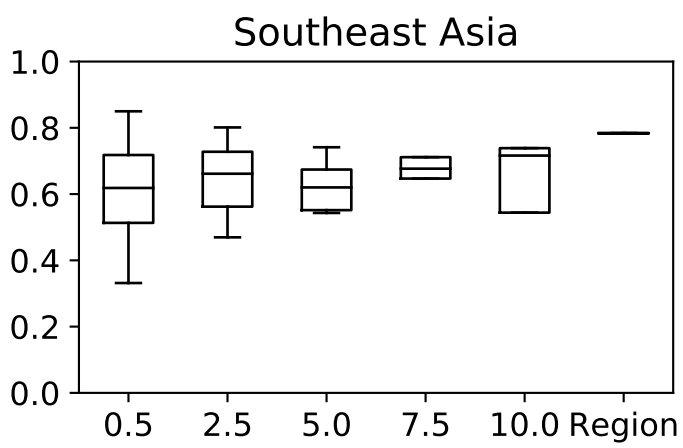
Southeast Asia
1.0
0.8
0.6
0.4
0.2
0.0
0.5
2.5
5.0
7.5
10.0
Region

Figure 4.

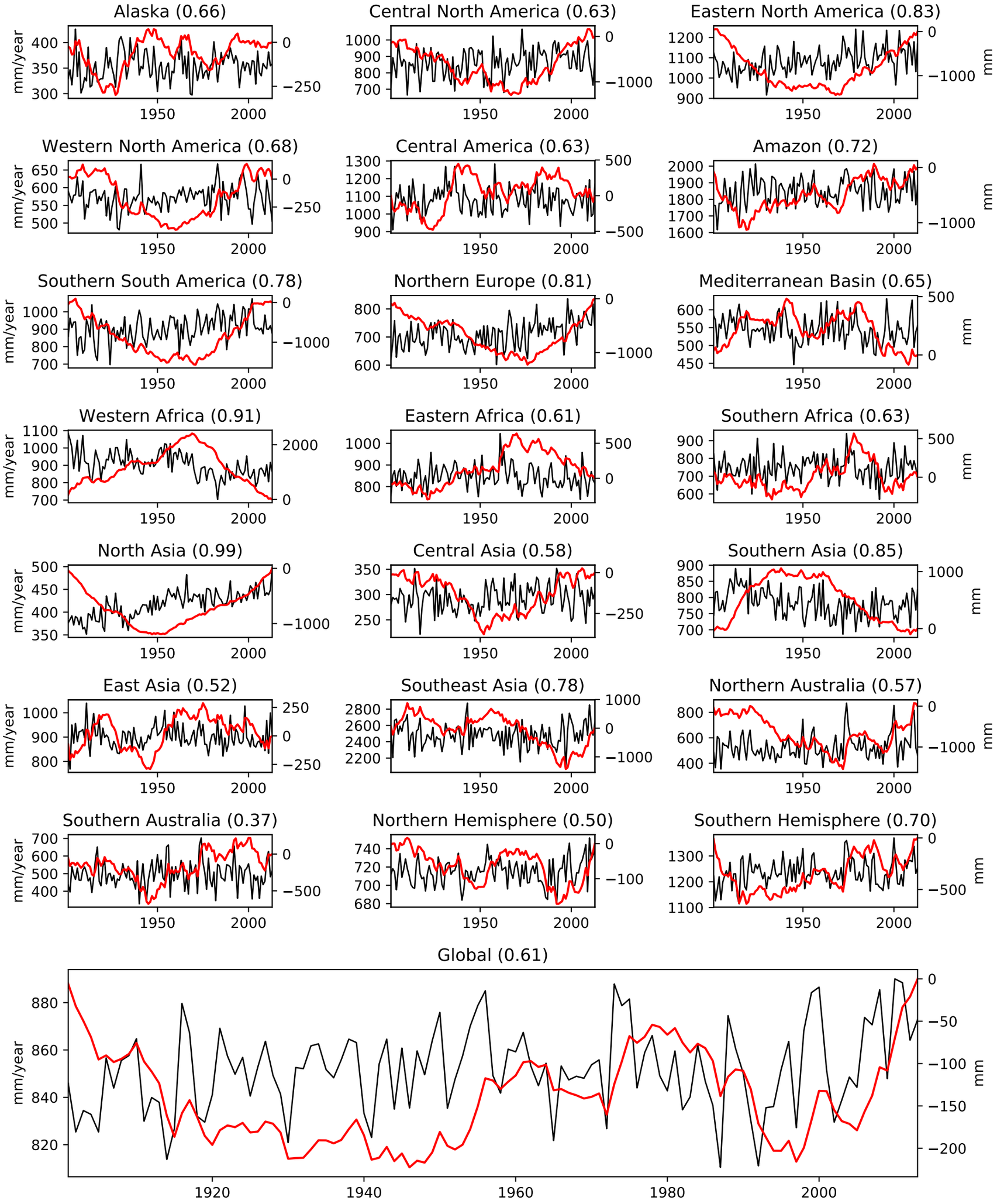
Alaska (0.66)
Central North America (0.63)
Eastern North America (0.83)
Western North America (0.68)
Central America (0.63)
Amazon (0.72)
Southern South America (0.78)
Northern Europe (0.81)
Mediterranean Basin (0.65)
Western Africa (0.91)
Eastern Africa (0.61)
Southern Africa (0.63)
North Asia (0.99)
Central Asia (0.58)
Southern Asia (0.85)
East Asia (0.52)
Southeast Asia (0.78)
Northern Australia (0.57)
Southern Australia (0.37)
Northern Hemisphere (0.50)
Southern Hemisphere (0.70)
Global (0.61)
mm/year
mm
1950
2000
1920
1940
1960
1980

Figure 5.

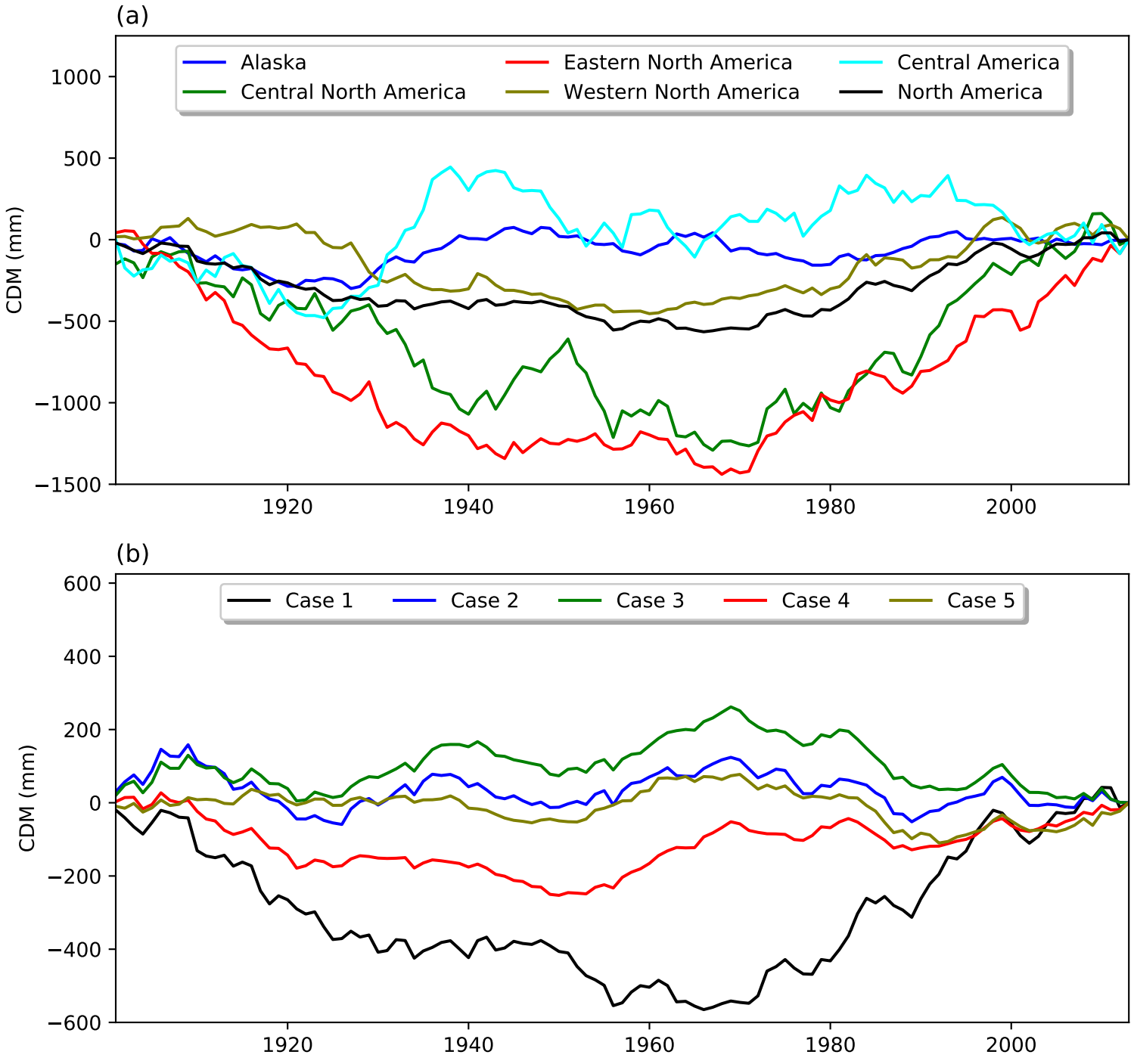
(a)
Alaska
Central North America
Eastern North America
Western North America
Central America
North America
CDM (mm)
1000
500
0
−500
−1000
−1500
1920
1940
1960
1980
2000
(b)
Case 1
Case 2
Case 3
Case 4
Case 5
CDM (mm)
600
400
200
0
−200
−400
−600
1920
1940
1960
1980
2000

Figure 6.

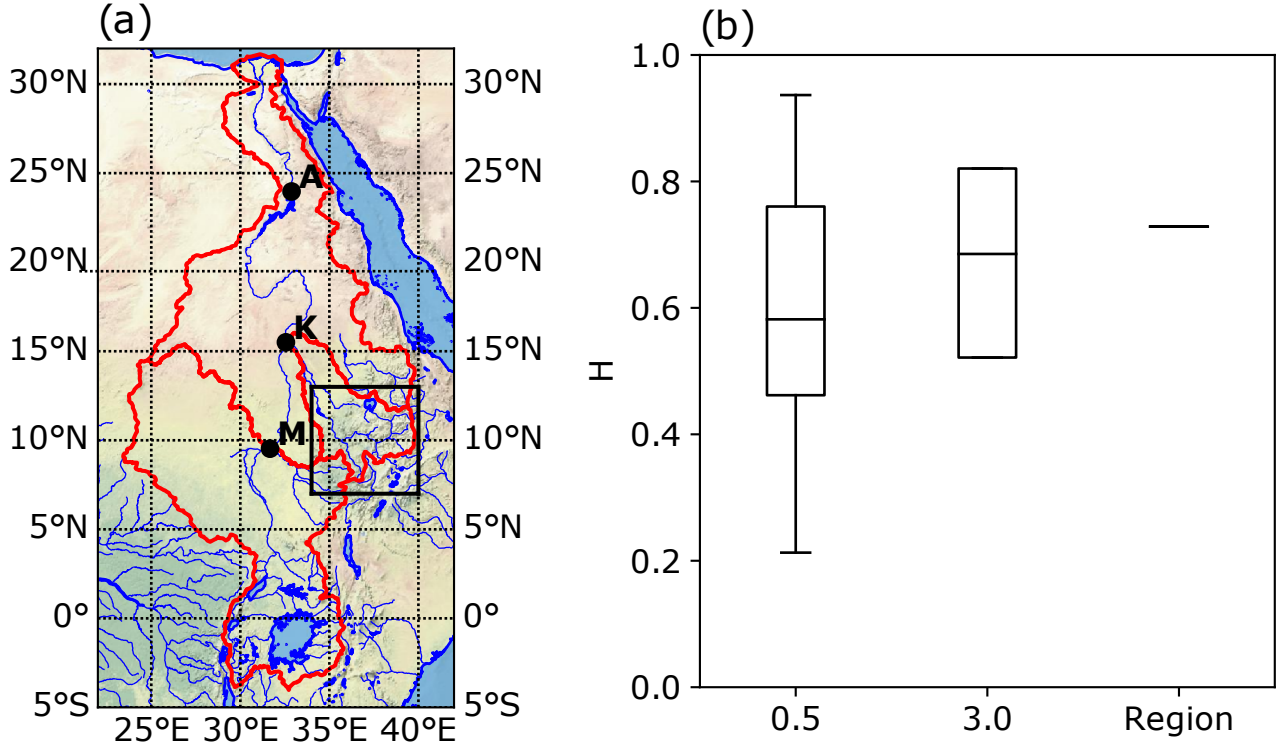
(a)
30°N
25°N
20°N
15°N
10°N
5°N
0°
5°S
25°E
30°E
35°E
40°E
A
K
M
(b)
H
1.0
0.8
0.6
0.4
0.2
0.0
0.5
3.0
Region

Figure 7.

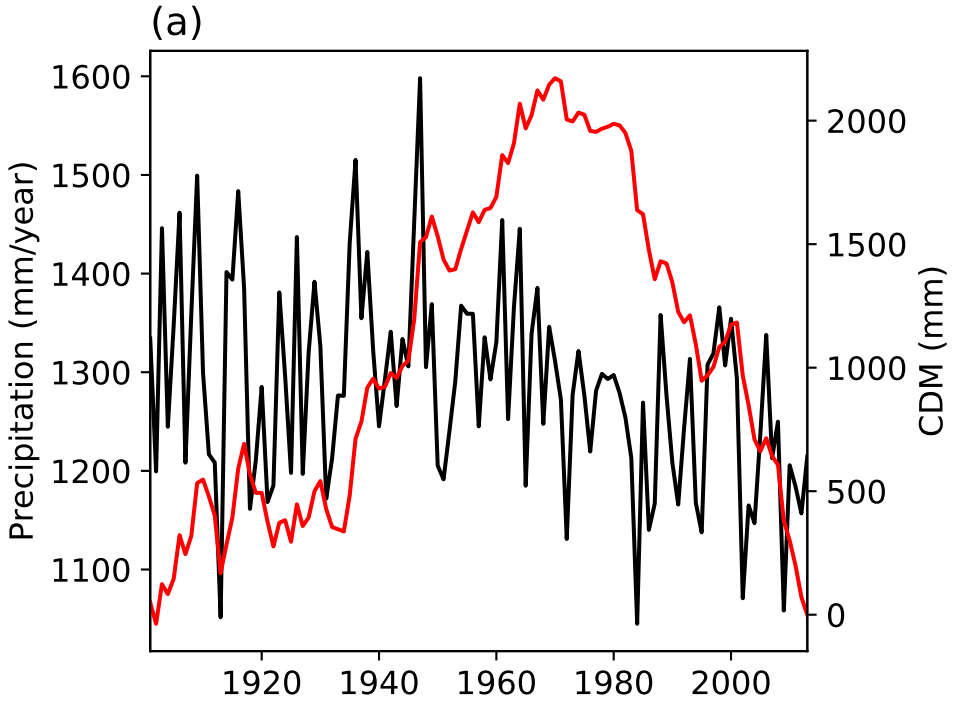
(a)
Precipitation (mm/year)
CDM (mm)
1600
1500
1400
1300
1200
1100
2000
1500
1000
500
0
1920
1940
1960
1980
2000

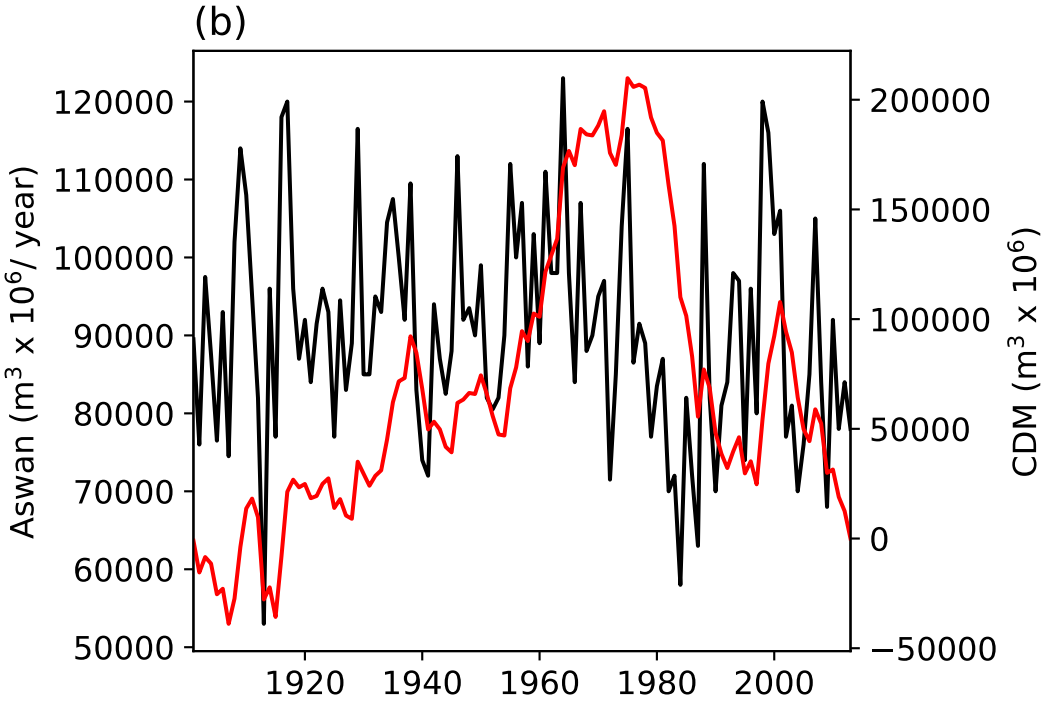
(b)
Aswan (m3 x 10^6/ year)
CDM (m3 x 10^6)
120000
110000
100000
90000
80000
70000
60000
50000
200000
150000
100000
50000
0
−50000
1920
1940
1960
1980
2000